



## Original Paper

## Spectral graph convolution networks for microbialite lithology identification based on conventional well logs



Ke-Ran Li <sup>a</sup>, Jin-Min Song <sup>a,\*</sup>, Han Wang <sup>a</sup>, Hai-Jun Yan <sup>b</sup>, Shu-Gen Liu <sup>a,c</sup>, Yang Lan <sup>d</sup>, Xin Jin <sup>a</sup>, Jia-Xin Ren <sup>a</sup>, Ling-Li Zhao <sup>a</sup>, Li-Zhou Tian <sup>a</sup>, Hao-Shuang Deng <sup>a</sup>, Wei Chen <sup>a</sup>

<sup>a</sup> State Key Laboratory of Oil and Gas Reservoir Geology and Exploitation, Chengdu University of Technology, Chengdu, 610059, Sichuan, China

<sup>b</sup> Research Institute of Petroleum Exploration and Development, Beijing, 100083, China

<sup>c</sup> Xihua University, Chengdu, 610039, Sichuan, China

<sup>d</sup> University College London, Gower Street, London, WC1E 6BT, UK

## ARTICLE INFO

## Article history:

Received 1 March 2023

Received in revised form

6 November 2024

Accepted 14 February 2025

Available online 17 February 2025

Edited by Jie Hao and Meng-Jiao Zhou

## Keywords:

Graph convolution network

Microbialite

Lithology forecasting

Well log

## ABSTRACT

Machine learning algorithms are widely used to interpret well logging data. To enhance the algorithms' robustness, shuffling the well logging data is an unavoidable feature engineering before training models. However, latent information stored between different well logging types and depth is destroyed during the shuffle. To investigate the influence of latent information, this study implements graph convolution networks (GCNs), long-short temporal memory models, recurrent neural networks, temporal convolution networks, and two artificial neural networks to predict the microbial lithology in the fourth member of the Dengying Formation, Moxi gas field, central Sichuan Basin. Results indicate that the GCN model outperforms other models. The accuracy, F1-score, and area under curve of the GCN model are 0.90, 0.90, and 0.95, respectively. Experimental results indicate that the time-series data facilitates lithology prediction and helps determine lithological fluctuations in the vertical direction. All types of logs from the spectral in the GCN model and also facilitates lithology identification. Only on condition combined with latent information, the GCN model reaches excellent microbialite classification resolution at the centimeter scale. Ultimately, the two actual cases show tricks for using GCN models to predict potential microbialite in other formations and areas, proving that the GCN model can be adopted in the industry.

© 2025 The Authors. Publishing services by Elsevier B.V. on behalf of KeAi Communications Co. Ltd. This is an open access article under the CC BY-NC-ND license (<http://creativecommons.org/licenses/by-nc-nd/4.0/>).

## 1. Introduction

With the paleoceanic and paleoenvironmental evolution in the Neoproterozoic-Paleozoic boundary, microbialite has been extensively developed in the terminal Ediacaran (Sinian) Dengying Formation. Rather than simply reflecting paleo-information, previous research indicates that microbialites are significant carbonate reservoirs for petroleum systems (Al-Siyabi, 2005; Collins et al., 2014; Grotzinger and Al-Rawahi, 2014; Jiang et al., 2018a, 2018b, 2019; Mancini et al., 2004, 2008; Smodej et al., 2019; Zou et al., 2014). Several factors contribute to the presence of excellent reservoirs in the Dengying Formation, including paleoclimate, sea-level fluctuations, geochemistry, and paleo-uplift (Yan et al., 2022). Among these factors, the existence of microbial mound-shoal complexes

and their spatial distributions on the carbonate platform are particularly important (Lan et al., 2022). The analysis of microbial mound-shoal complexes heavily relies on petrological analysis of microbialites in numerous individual wells. To determine their distribution, well profiles based on petrological sequence establishment serve as crucial data for constraining the spatial distributions of microbial mound-shoal complexes. The fundament of well profiles is the petrological sequence in each single well. Precise petrological analysis in wells plays a pivotal role in hydrocarbon exploration for microbial mound-shoal complexes.

Core observation, thin-section analysis, and logging interpretation are common used methods in petrologic analysis. Core observation analyses are limited due to the high cost associated with borehole drilling. Lithological interpretation from conventional logging data is widely used in the petroleum industry. However, interpreting microbial carbonate lithology poses challenges. Cross-plotting analysis and imaging logs are frequently employed for predicting microbialite lithography (Feng et al., 2021).

\* Corresponding author.

E-mail address: [songjinmin2012@cdut.edu.cn](mailto:songjinmin2012@cdut.edu.cn) (J.-M. Song).

Imaging logs are scarce and costly compared to the abundant and inexpensive conventional logs. Simultaneously, the complexity of logging curves limits the interpretation accuracy of the cross-plotting analysis. Furthermore, cross-plotting analysis relies on manual operations and is time-consuming. The economic and technical limits the exploration of the deeply buried microbialite reservoirs in the Dengying Formation. To reduce costs and improve prediction accuracy, an automated technical flow for processing conventional data logging is crucial for identifying microbialites in the Dengying Formation. The rapid development of machine learning algorithms in recent decades provides new perspectives on constructing the technical flow.

A variety of machine learning algorithms have been widely utilized in the field of oil and gas exploration, including the XGBoost model, physics-informed neural networks (PINN), artificial neural networks and some statistical machine learning models (Busch et al., 1987; Wang and Carr, 2012; Bhattacharya et al., 2016; Ghosh et al., 2016; Xie et al., 2018; Barbosa et al., 2019; Bressan et al., 2020; Chen et al., 2020; Liu et al., 2021; Tang et al., 2014; Xu et al., 2021; Zhang et al., 2022). In the context of lithology/lithofacies classification, machine learning techniques have proven to be effective in interpreting logging data and achieving satisfactory performance (Rogers et al., 1992; Bhatt and Helle, 2002; Dubois et al., 2007; Hall, 2016). However, most previous studies have overlooked the importance of preserving the temporal information inherent in logging data during the process of supervised learning. Recently the time-series information has got attention and been demonstrated by a specific study (Hilborn, 2000; Zeeden et al., 2023) that well logging data exhibit chaotic time-series characteristics, and shuffling the data can lead to the loss of valuable temporal patterns.

The concept of time-series is widely used in cyclic stratigraphy. Worthington (1990) conducted the initial research on time-series data in well logging within the context of cyclic stratigraphy. Worthington (1990) referred to the time-series information as sediment cyclicity. Algeo (1993) quantified the relationship between stratigraphy and the terminology of time-series using paleomagnetic data. Prokoph (1999) and Prokoph and Barthelmes (1996) discussed the impact of stratigraphic parameters on geological time-series data and highlighted the ability of sedimentation successions to capture abrupt sedimentary changes.

After successfully being utilized in cyclic stratigraphy, time-series data have generated the interest of scientists working with well logging data. Verma et al. (2014) inputted logging data in a time-series form and compared the similarity among well logs using the synchronization likelihood method. Recently, with the rapid development of sequential neural network models, including the recurrent neural network model (RNN, Zaremba et al., 2014), long-short temporal memory model (LSTM, Hochreiter and Schmidhuber, 1997; Graves, 2012), gate recurrent unit model (GRU, Cho et al., 2014), and temporal convolutional network (TCN, Bai et al., 2018), time-series information has been adopted by well logging data scientists. For instance, Feng (2021) utilized a transferred BiLSTM model to identify lithology from logging data and verified the effectiveness of time-series consequence features in lithological forecasting. LSTM models (Shan et al., 2021; Romanenkov et al., 2022) can extract latent information from logs and boosted the down-stream logging interpreting tasks. Song et al. (2023) established a time-domain random forests model to generate well logs. In summary, LSTM and other sequential neural network models can effectively finishing interpreting tasks via the time-series information from well logging and achieved great performance in several down-stream tasks like drilling monitoring (Zhang et al., 2023), logs generation (Wang et al., 2022; Song et al., 2023), lithofacies/lithology prediction (Aftab et al., 2023;

Carrasquilla, 2023; Dong et al., 2023a,b), reservoir/fracture identification (Dong et al., 2023a,b; Yang et al., 2023), strata parameters predictions (Souza et al., 2022; Zhang et al., 2022; Chen et al., 2023; Kannaiah and Maurya, 2023; Wan et al., 2023).

While recent models have shown advancements in time-series processing, the presence of long or short time-dependence in actual sequential data can undermine accurate time-series forecasting. Moreover, the relations among different well logs and the way to modeling did not get fully consideration. To build models that handle time-series data with multiple types of well logs, this research introduces a novel graph data and graph convolution neural networks (GCNs) to further investigate the way to fully dig up the latent information in well logs.

This paper aims to assess the advantages of incorporating time-series and spectral information by utilizing GRUs and a self-attention mechanism to transform logging data into graph data. Additionally, the convolution process on graph data (GCN) is introduced. The performance of various models including GCN, LSTM, RNN, TCN, fully connected artificial neural networks (ANNs), and Dropout-ANN models are then compared. To further investigate the impact of different blocks in GCN, ablation experiments are conducted to evaluate their contributions. At last, we paid attention to the industry application and showed two cases about how to fast employ the trained GCN models in other formations by transfer learning. Our research findings indicate that the GCN model can enhance lithology prediction and has potential for accelerating petroleum exploration through microbialite classification. The workflow of this paper is shown in Fig. 1.

## 2. Geological background

This study was exhibited on logging data and corresponding lithological labels from the fourth member of Ediacaran Dengying Formation, Moxi gas field. The Moxi gas field, situated in the central part of the Sichuan Basin (Fig. 2(a), (b), (c)), is part of the larger Gaoshiti-Moxi gas field (Anyue gas field) (Wei et al., 2014). The Dengying Formation ( $Z_{2dn}$ ) consists of four members, namely  $Z_{2dn_1}$  –  $Z_{2dn_4}$  (Fig. 2(d)). The  $Z_{2dn_2}$  and  $Z_{2dn_4}$  members contain abundant cyanobacteria, primarily in the form of stromatolite and thrombolite fabrics (Fig. 2(d)). The first member consists of dolostone with minimal microbial fabrics, while the third member comprises shale and silty sandstone (Fig. 2(d)). The lithological interpretation of microbialite is vital and challenging for the hydrocarbon exploration in  $Z_{2dn_2}$  and  $Z_{2dn_4}$  members. The main exploring targets in the microbialite reservoir are five types, including:

### (1) Dolomicrite (MICR)

The dolomicrite exhibits a dark color with rare depositional structure in the core observation (Fig. 3(a)). Microscopic analysis (Fig. 3(b)) reveals that the primarily putty crystal dolomite and some powder crystal dolomite are the main depositions of the dolomicrite.

### (2) Stratiform stromatolite (SSTR)

The formation of the stratiform stromatolite related to the microbial deposits, especially for the microbial mats. Microbial mats are formed through the active metabolism of cyanobacteria (Zhu et al., 2020, 2022). The microbial mats are manifested as abundant parallel and laminated stripes on the drilling cores (Fig. 3(c), red frame). On the mesoscopic scale, the stratiform stromatolite (Fig. 3(c), red frame) tend to co-develop with wavy stromatolite (Fig. 3(c), yellow frame). On the microscopic scale, the

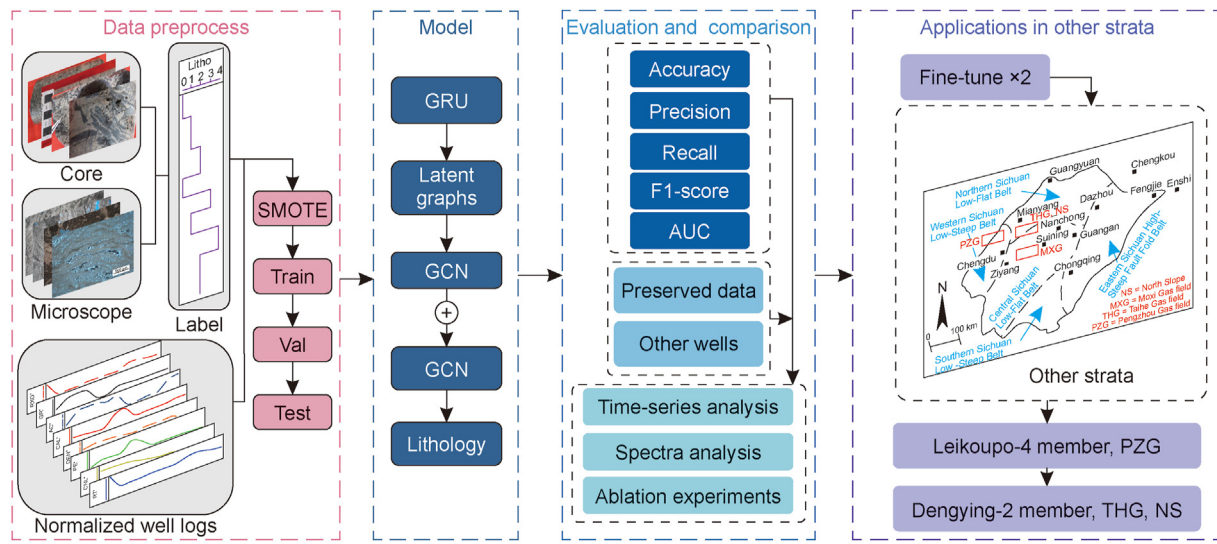


**Fig. 1.** Workflow of this study.

stratiform stromatolite exhibits intermittent dark lines (Fig. 3(d)) and the superimposition of continuous dark lines (Fig. 3(d)). Most pores are filled by fine crystal dolostone (Fig. 3(d)).

### (3) Wavy stromatolite (WSTR)

The origin of wavy stromatolite is closely associated with cyanobacteria. From the microscopic analysis, the wavy stromatolite exhibits dense and dark laminations with a large curvature (Fig. 3(e)), semi-circle structure (Fig. 3(f)), and superimposing from bottom to the top (Fig. 3(f)). Microscopically, a significant number of pores developed along the direction of strips at the interlayer positions (Fig. 3(g)). Wavy stromatolites tend to exhibit the development of primary pores and some dissolving pores tend to develop in the wavy stromatolite (Tang et al., 2022; Zhu et al., 2020, 2022; Fig. 3(g), red frame). Wavy stromatolite shows significant reservoir potential.

### (4) Thrombolite (THRO)

Similar to stromatolites, the thrombolite has been proven that the formation of thrombolites is closely linked to bacterial metabolism. Core observational analyses reveal that thrombolites exhibit distinct dark clots (indicated by yellow and red arrows in Fig. 3(h) and (i)), in contrast to the layered or laminated appearance of stromatolites. Under microscopic examination, thrombolites appear as densely packed dark clots (Fig. 3(j)). These clots mainly exhibit diffusing clots (indicated by red arrows in Fig. 3(j)). The formation of pores in thrombolites occurs through dissolution (blue part, Fig. 3(j)), showing great potential for reservoir development.

### (5) Siliceous stromatolite (SILIS)

The siliceous stromatolite is a lithological variation mostly found in the fourth member of the Dengying Formation. The siliceous stromatolite closely resembles the stratiform stromatolite, as both exhibit curved stocking strips (Fig. 3(k)). Microscopically, the main distinction lies in the development of quartz primarily at the interlayers (Fig. 3(l)). Additionally, quartz crystallization occurs at the interlayer fractures (Fig. 3(l)). The presence of quartz in the siliceous stromatolite does not significantly enhance reservoir pore quality. Nevertheless, due to their brittleness, the quartz-rich layers

are suitable for fracturing during development (Yarali and Kahraman, 2011). Furthermore, the siliceous stromatolite is found adjacent to high-quality reservoirs such as thrombolite and wavy stromatolite. These neighboring layers can undergo hydrofracturing and generate fractures.

## 3. Data and methods

### 3.1. Logs preprocessing and latent information modeling

A total of 44 wells containing continuous microbial depositing sequences in  $Z_2dn_4$  were selected from the Moxi gas field (two wells are preserved, without training). To assess the log integrity across the wells, eight types of logs were chosen: acoustic log (AC), caliper well log (CAL), compensated neutron log (CNL), density log (DEN), gamma-ray log (GR), photoelectric absorption cross-section index log (PE), deep lateral resistivity log (RLD), and shallow resistivity log (RLLS). Prior to lithology forecasting, data preprocessing is performed using the method proposed by Zheng et al. (2022), involving three steps: (1) depth calibration, (2) removal of invalid values, and (3) normalization. A total of 10,367 valid data points (from 42 wells, logging data with labels) were collected. These labels of lithofacies were collected based on petrologies, sedimentary textures and structures, depositing patterns of the lithology from cutting descriptions, core observations and microscopic analysis. In this research, labels interpreted by terms of the shapes of log curves where no cuttings or cores are avoidable to ensure the high quality of the labels. Cross-plotting analysis reveals the relationships between two logs and a significant overlap in data distribution (Fig. (4)). Fig. 5(a) indicates an imbalanced data distribution. To address this issue, the synthetic minority over-sampling technique (SMOTE) algorithm (details can be seen in Table 1), as shown in Fig. 5(b) (Chawla et al., 2002), was employed and yielded 12570 data for training.

From the knowledge of sedimentology, the depth represents the sedimentary time points in geological history. Based on this, continuous logging data can be considered a time-series sequence, similar to temperature fluctuations over years. Similarly, information is also concealed within the different types of logs. Manual logging interpretation involves comparing and interpreting different logs. For instance, Passey et al. (1990) proposed the AlogR index, which is calculated by the difference between the resistivity and sonic logs, to predict the TOC. Therefore, comparisons among

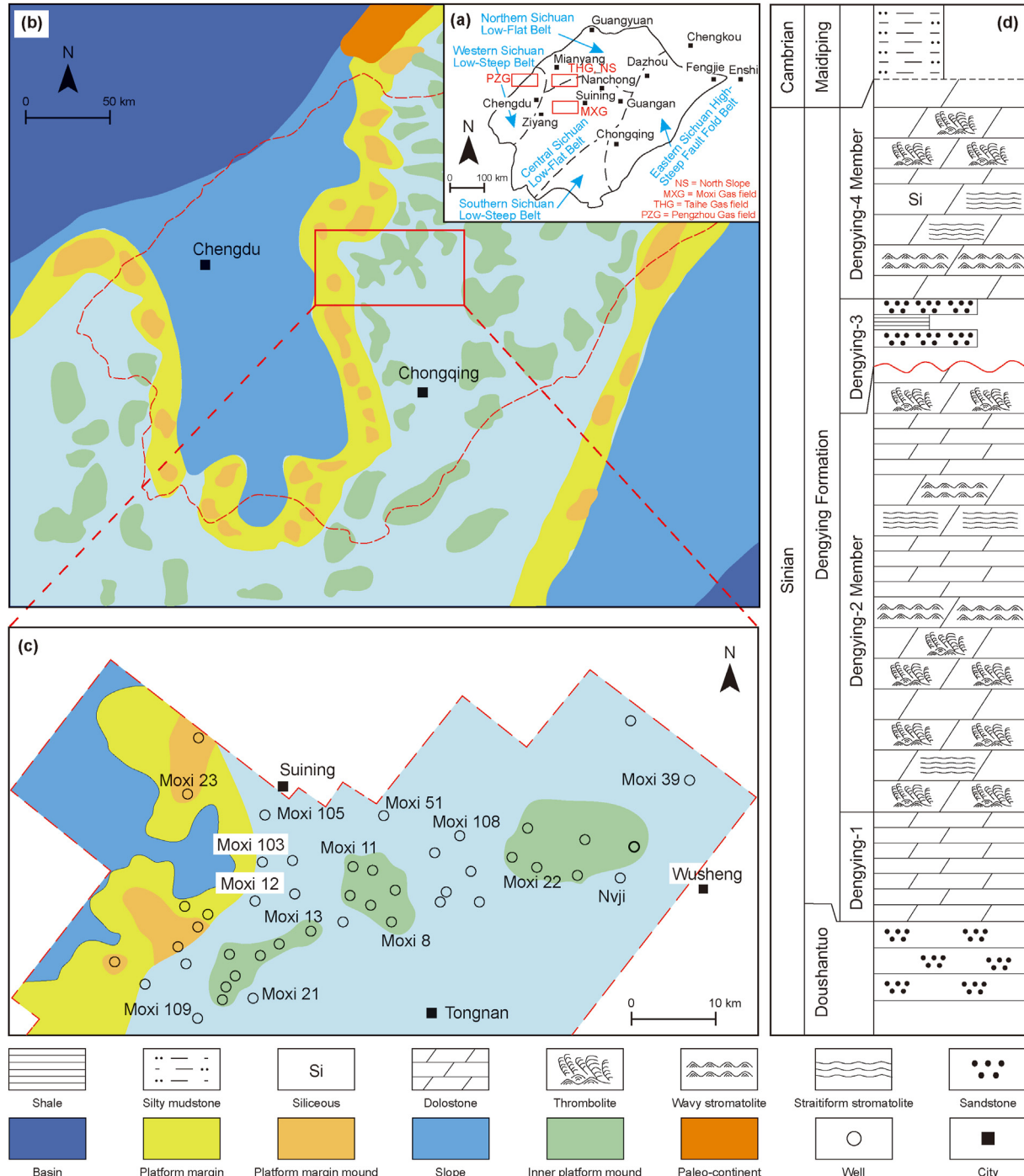


**Fig. 2.** Locations, paleogeography map, research areas and simplified stratigraphic column of the Moxi gas field central Sichuan basin. **(a)** The locations of Moxi gas field, central Sichuan basin, Taihe gas field, north slope of central Sichuan basin and Triassic Pengzhou gas field, west Sichuan basin (The Moxi gas field is the main research area. The Taihe gas field and Pengzhou gas field are the experimental research areas, which are introduced to test the model's ability of fast employment in other formations); **(b)** the paleogeography map of the fourth member of Dengying Formation (Modified from Liu et al., 2017; L. Wang et al., 2020; Liu et al., 2021), the red dotted line is the boundary of Sichuan Basin and the red square is the study area; **(c)** the location and wells distribution of Moxi gas field; **(d)** the stratigraphic column of the Dengying Formation (Modified from Zhu et al., 2020).

different logs are beneficial for interpretations. To capture latent information, this study disregards traditional correlation analysis and treats logs as a complete spectrum. As the sampling window moves, a series of spectra forms a time-series sequence in the vertical direction (Fig. 6(a)). After the gate recurrent unit (GRU) processing (Fig. 6(b) and (c)), the depth-series spectral data are transformed into latent graphs.

### 3.2. Gate recurrent unit

The gate recurrent unit (GRU) is a simplified long short-term memory (LSTM) model used for processing time-series information (Cho et al., 2014). The GRU block consists of multiple GRU models, with a self-attention mechanism added to the final GRU (Fig. 7(a)).

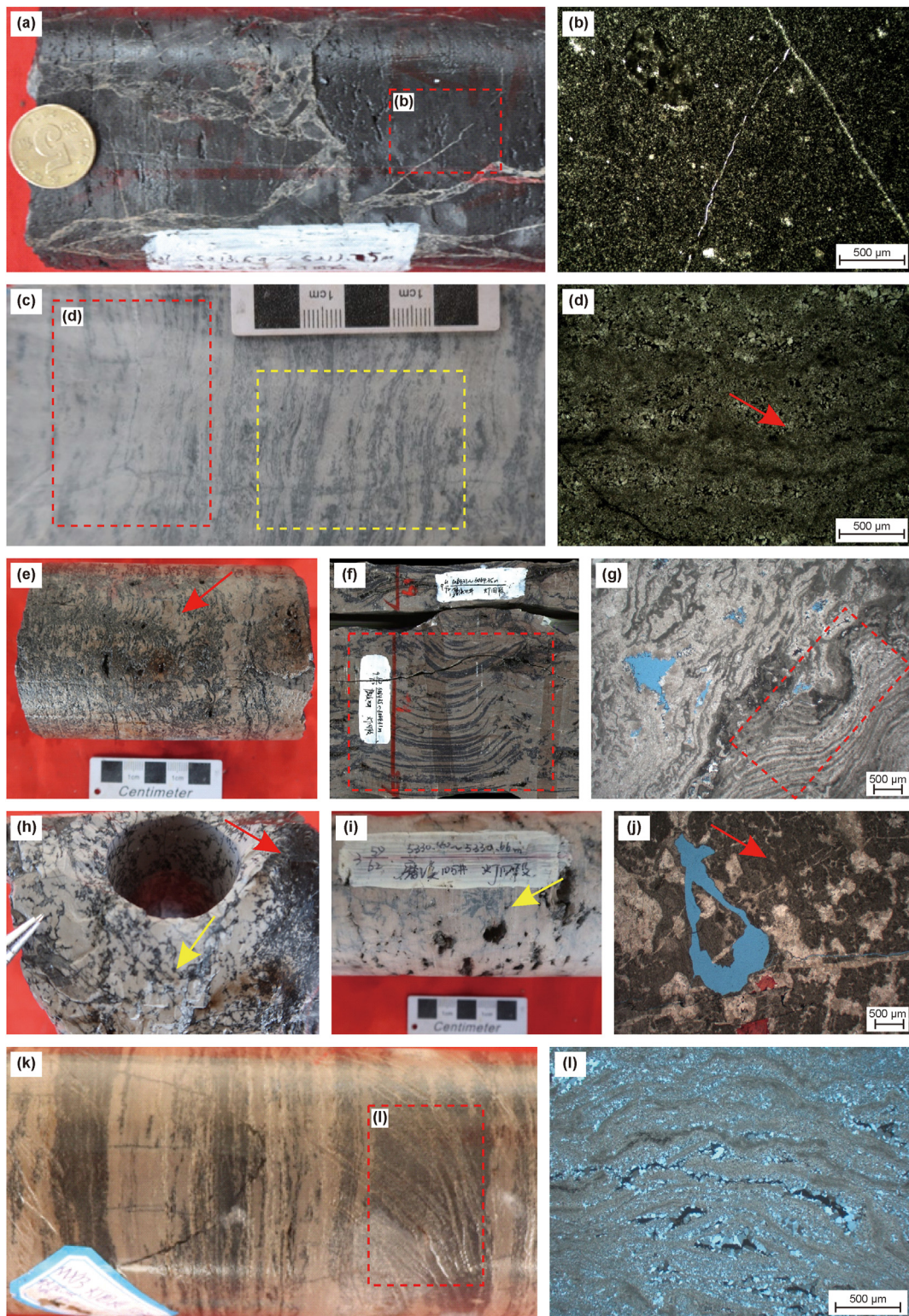


**Fig. 3.** The petrological features of the Dengying-4 Member in the Moxi gas field by mesoscopic and microscopic analysis. (a) Dark dolomitic with breccia developed, Moxi 23; (b) putty–powder crystal dolomite, Moxi 23; (c) light gray dolomitic, stratiform stromatolite develops in the upper part (red frames) and waery stromatolite develops in the lower part (yellow frame), Moxi 105; (d) putty crystal dolomite, continuous and vertical stocking stromatolite developed (red arrow), Moxi 105; (e) light gray wavy stromatolite (red arrow), Moxi 105; (f) core scanning image of wavy stromatolite (red frame), Moxi 21; (g) putty crystal dolomite, microbialite strips stocked and bend with a large curvature that forms a semi-circle structure (red frame), pores developed (blue part), Moxi 108; (h) mid gray thrombolite, diffusing clots (yellow arrow); (i) mid gray thrombolite, diffusing clots (yellow arrow), semicircular spherical clots (red arrow), Moxi 105; (j) mid gray thrombolite, diffusing clots (yellow arrow), semicircular spherical clots (red arrow) developed, Moxi 22; (k) siliceous stromatolite (red frame), Moxi 13; (l) siliceous stromatolite, Moxi 105.

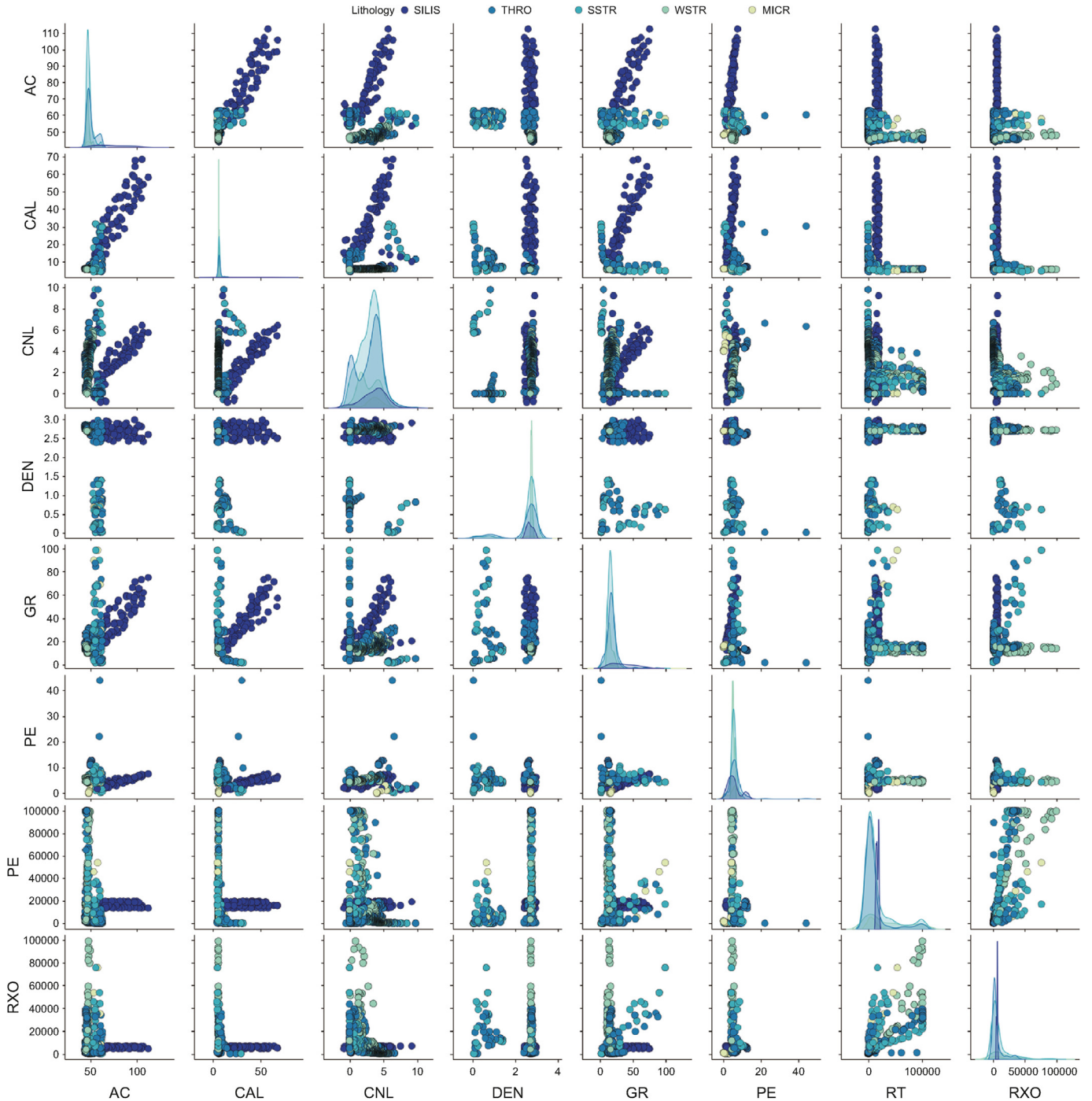


**Fig. 4.** Cross-plot of well logs and corresponding lithological labels in Moxi gas field, central Sichuan basin (From 44 wells).

Let  $\mathbf{X}$  represents the logging data,

$$\mathbf{X} = \begin{pmatrix} x_{11} & x_{12} & \cdots & x_{18} \\ x_{21} & x_{22} & \cdots & x_{28} \\ \vdots & \vdots & \ddots & \vdots \\ x_{n1} & x_{n2} & \cdots & x_{n8} \end{pmatrix} \quad (1)$$

$x_{ij}$  represents log data from log type  $j$ , where  $i$  denotes the depth of log data.

The spectra in depth  $d$ , denoted as  $\mathbf{s}_d$ , is composed of eight horizontal logs.

$$\mathbf{s}_d = (x_{d1} \ x_{d2} \ \cdots \ x_{d8}) \quad (2)$$

Each depth's spectra enter an independent GRU (Fig. 7(a)) and generates a corresponding hidden state  $h$ . An attention mechanism is added in the last GRU to produce the adjacent matrix and produce the graph eventually (Fig. 7(a)).

The GRU has two gates: the reset gate  $rt$  and the update gate  $Z_t$ . The spectra from depth  $d$  and window  $t$  are multiplied the matrix  $W_{(z)}$ , while the hidden state of time step  $t-1$  is multiplied by the matrix  $U_{(z)}$ . Both  $W_{(z)}$  and  $U_{(z)}$  are data-driven. The sum of these two parts is then passed through a sigmoid function and  $Z_t$  is reached

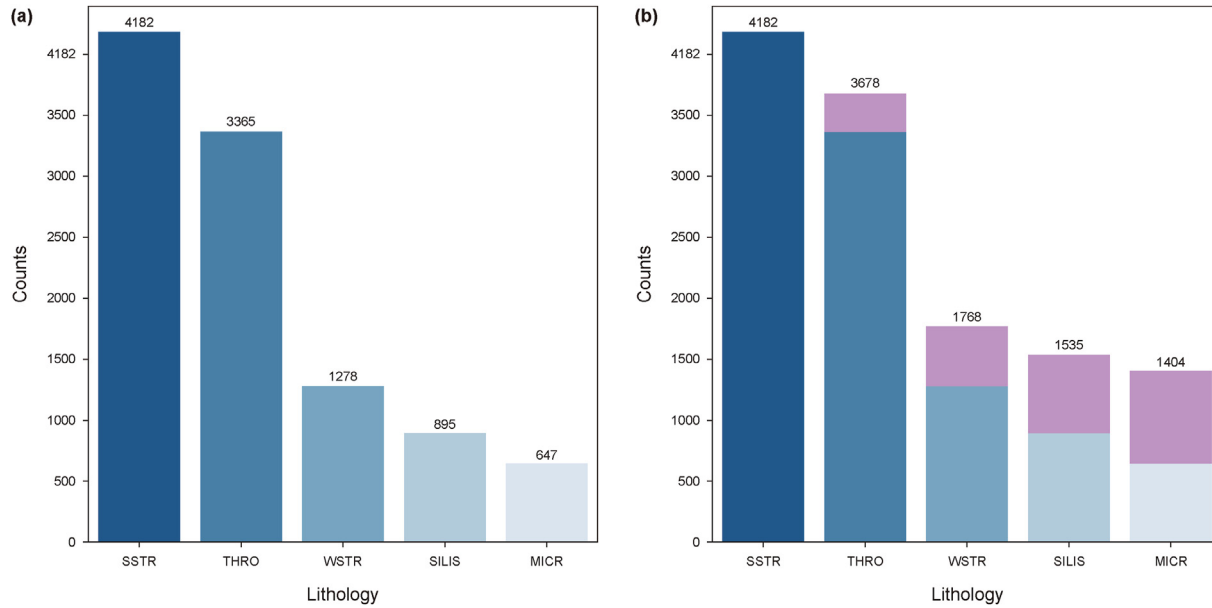


**Fig. 5.** Distributions of the lithological labels in Moxi gas field, central Sichuan basin (SSTR = stratiform stromatolite; THRO = thrombolite; WSTR = wavy stromatolite; SILIS = siliceous stromatolite; MICR = dolomiticrite; without two preserved wells, from 42 wells). (a) Original labels distribution; (b) the label distribution after data augmentation (dark pinks represent the counts of the data augmentation) by SMOTE (Chawla et al., 2002).

**Table 1**

The pseudocode of SMOTE algorithm.

**Algorithm synthetic minority over-sampling technique (SMOTE) ( $N, k$ )**

**Input:**

Minority Class Samples: List of minority class samples  
N: Percentage of SMOTE (e.g., 100% would double the minority class size)  
k: Number of nearest neighbors to use for synthetic sample generation

**Output:** Synthetic Samples: List of synthetic samples generated

```

1: Initialize Synthetic Samples as an empty list
2: Calculate  $N'$  # the smallest integer greater than or equal to  $N/100$ 
3: for each sample  $x$  in Minority Class Samples do
4:   Find  $k$  nearest neighbors of  $x$  using Euclidean distance
5:   for  $i$  from 1 to  $N'$  do
6:     Randomly select one of the  $k$  nearest neighbors # call it  $nn$ 
7:     Generate a synthetic sample  $s$  by interpolating between  $x$  and  $nn$ :
8:     for each feature  $f$  in  $x$ , calculate the difference  $df = nn[f] - x[f]$ :
9:     Multiply  $df$  by a random number between 0 and 1, call this  $delta$ 
10:    The synthetic feature value  $s[f] = x[f] + delta$ 
11:    Add the synthetic sample  $s$  to Synthetic Samples
12:   end for
13: end for
14: end for

```

(Fig. 7(b)). The procedure can be represented as

$$z_t = \text{sigmoid}(W_{(z)} \times x_t + U_{(z)} \times h_{t-1}) \quad (3)$$

The reset gate ( $r_t$ ) functions to select the information to be ignored. It has similar formulation like  $Z_t$ . The formula of  $r_t$  is

$$r_t = \text{sigmoid}(W_{(r)} \times x_t + U_{(r)} \times h_{t-1}) \quad (4)$$

With the calculated  $r_t$  and  $Z_t$ , a new memory unit,  $h_t'$  is computed using

$$h_t' = \tanh(W_{(h)} \times x_t + r_t \odot U_{(h)} \times h_{t-1}) \quad (5)$$

The output of GRU,  $h_t$ , will be updated by

$$h_t = z_t \odot h_{t-1} + (1 - z_t) \odot h_t' \quad (6)$$

$h_t$  represents the hidden layer of last state of GRU. Due to the sequential input of spectra in a window, the time-series information is transferred into  $h_t$ . The adjacent matrix  $W$  is then calculated by the self-attention mechanism (Fig. 7(a)). The  $W$  is derived from the self-attention mechanism as follows.

$$Q = W_{(z)} W_{(r)}, K = W_{(z)} W_{(h)}, V = \text{softmax}\left(\frac{QK^T}{\sqrt{d}}\right) \quad (7)$$

In the formula,  $Q$  and  $K$  represent the query and key in the self-attention mechanism, respectively.  $W_{(z)}$ ,  $W_{(r)}$ , and  $W_{(h)}$  are learnable parameters in Eqs. (3)–(5).  $d$  denotes the size of  $h_t$ . The dimension of the resulting matrix  $W$  is  $n \times n$ , where  $n$  represents the number of log types ( $n = 8$  in this case).

### 3.3. Graph convolution network block

Graph convolution differs from convolution operations in convolution neural networks (CNNs) and other neural networks. Graph convolution relies on Laplacian transformation and graph Fourier transform (Fig. 8).

The adjacent matrix gained by GRUs are the basis of Laplacian transformations. The adjacent matrix  $W$  is input into the graph Fourier transform block and get the Laplacian feature vector  $L$  (Cao et al., 2020, Fig. 8). Subsequently,  $L$  undergoes processing through discrete Fourier transform (DFT). DFT is defined as

$$L_{\text{DFT}} = \sum_{n=0}^{N-1} L \cdot [\cos(2\pi mn / N) - j \cdot \sin(2\pi mn / N)] \quad (8)$$

where  $m$  represents the frequency domain signal with  $m \in [0, 7]$ ,  $n$  represents the number of time-domain discrete signals with  $n \in [0, 7]$ , and  $N$  represents the number of log types, specifically  $N = 8$ .

The  $L_{\text{DFT}}$  is convoluted in one dimension and then enters the subsequent gated linear unit (GLU). The GLU is defined as

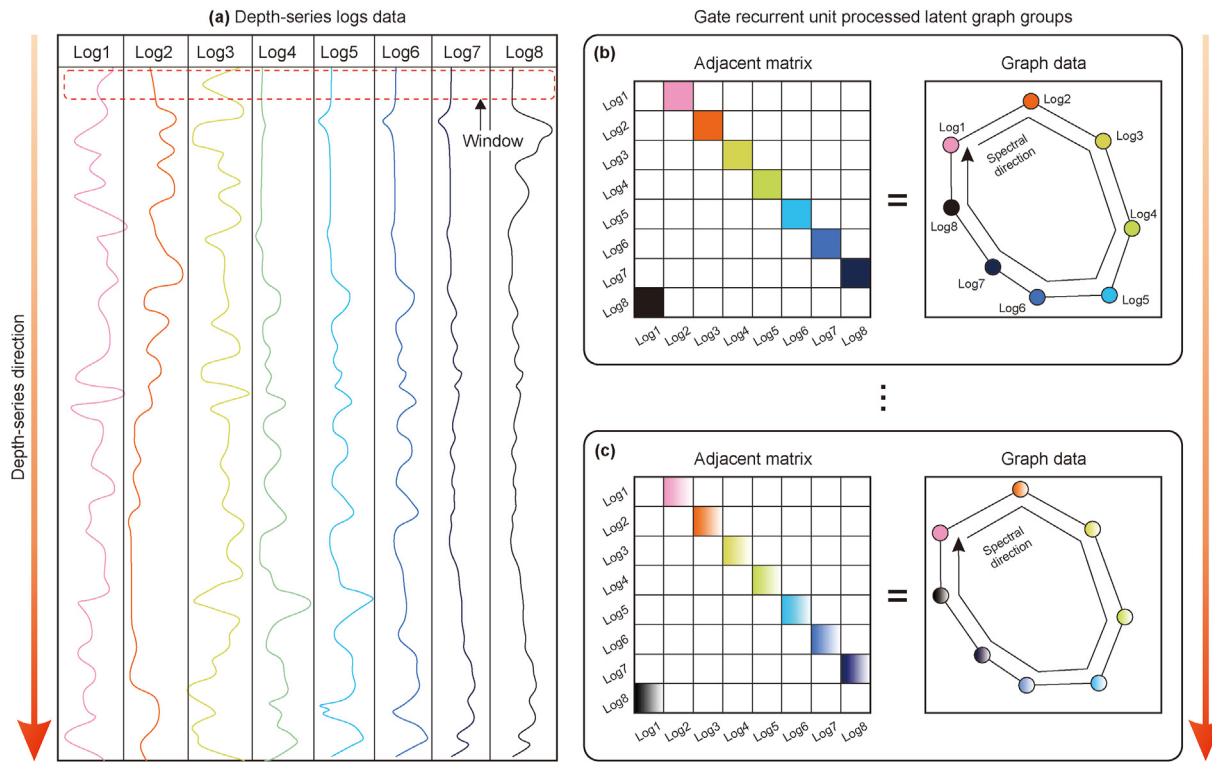


**Fig. 6.** Diagram of the process of extracting logging data and transmitting to latent graphs via sampling window. **(a)** Graphic representation of actual logging data; **(b)** diagrammatic of the latent graph from the first spectra in the sampling window; **(c)** diagram of the latent graph from the last spectra in the sampling window.

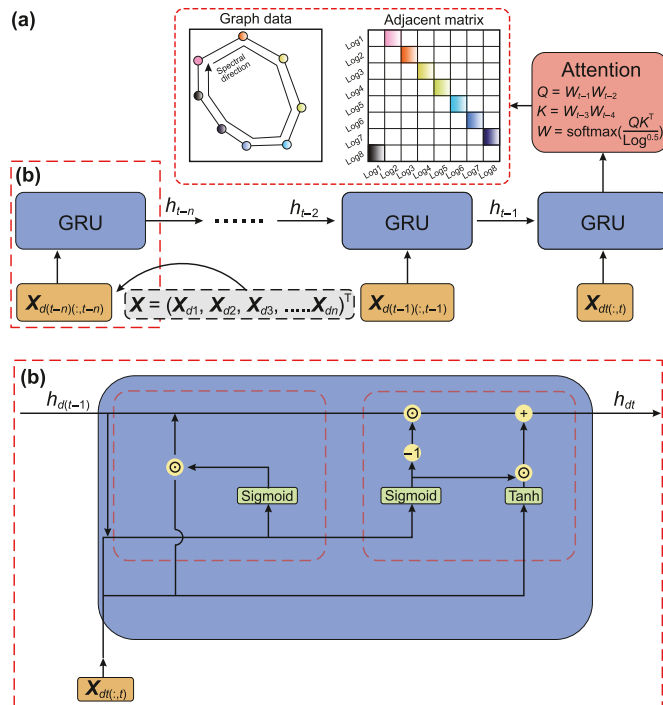


**Fig. 7.** Workflow of graph generating. **(a)** Graph generating by a series GRU and a self-attention block; **(b)** diagram of GRU (Modified from Cho et al., 2014).

$$\text{GLU}(L_{\text{DFT}}) = (L_{\text{DFT}} \times W_{\text{GLU}} + b_{\text{GLU}}) \otimes (L_{\text{DFT}} \times V_{\text{GLU}} + c_{\text{GLU}}) \quad (9)$$

where  $W_{\text{GLU}}$ ,  $b_{\text{GLU}}$ ,  $V_{\text{GLU}}$ , and  $c_{\text{GLU}}$  are learnable parameters.

Prior to graph convolution,  $\text{GLU}(L_{\text{DFT}})$  should be processed by inverse discrete Fourier transform ( $i_{\text{DFT}}$ ) to reconstruct the degree matrix  $\mathbf{D}$ , adjacent matrix  $\mathbf{A}$ , and Laplacian matrix  $\mathbf{L}$ .

$$\mathbf{L} = \mathbf{D} - \mathbf{A} \quad (10)$$

Sampling feature maps using images kernels provides a unique example for graph convolution. The key distinction between graph convolution and image convolution lies in the connectivity of vertices, where not all vertices are connected, unlike the pixels in images are all connected. Employing the kernel method in graph domain poses challenges. In order to access the information of adjacent vertices, graph convolution is defined as

$$\mathbf{H}^{l+1} = \sigma(\mathbf{L}\mathbf{H}^l\mathbf{W}^l) \quad (11)$$

Here,  $\mathbf{H}$  represents the hidden layer,  $\sigma$  is the nonlinear activate function, and  $\mathbf{W}^l$  signifies the matrix parameters of hidden layer  $l$ .

In order to enhance the impact of the self-degree of graphs,  $\mathbf{L}$  can be substituted with symmetric normalized Laplacian matrix  $\mathbf{L}_{\text{sym}}$ .

$$\mathbf{L}_{\text{sym}} = \mathbf{D}^{-\frac{1}{2}}\mathbf{A}^{\sim}\mathbf{D}^{-\frac{1}{2}} = \mathbf{D}^{-\frac{1}{2}}(\mathbf{D} - \mathbf{A})\mathbf{D}^{-\frac{1}{2}} \quad (12)$$

Following feature mapping through graph convolution, the data flow must be flattened. The flattened data is then subjected to softmax regression to output lithologies.

### 3.4. Evaluation

This paper introduces a novel loss function for the GCN Block. The loss function consists of two components. The first part evaluates the variation of  $X_{\text{in}}$  and  $X$  using mean squared error.

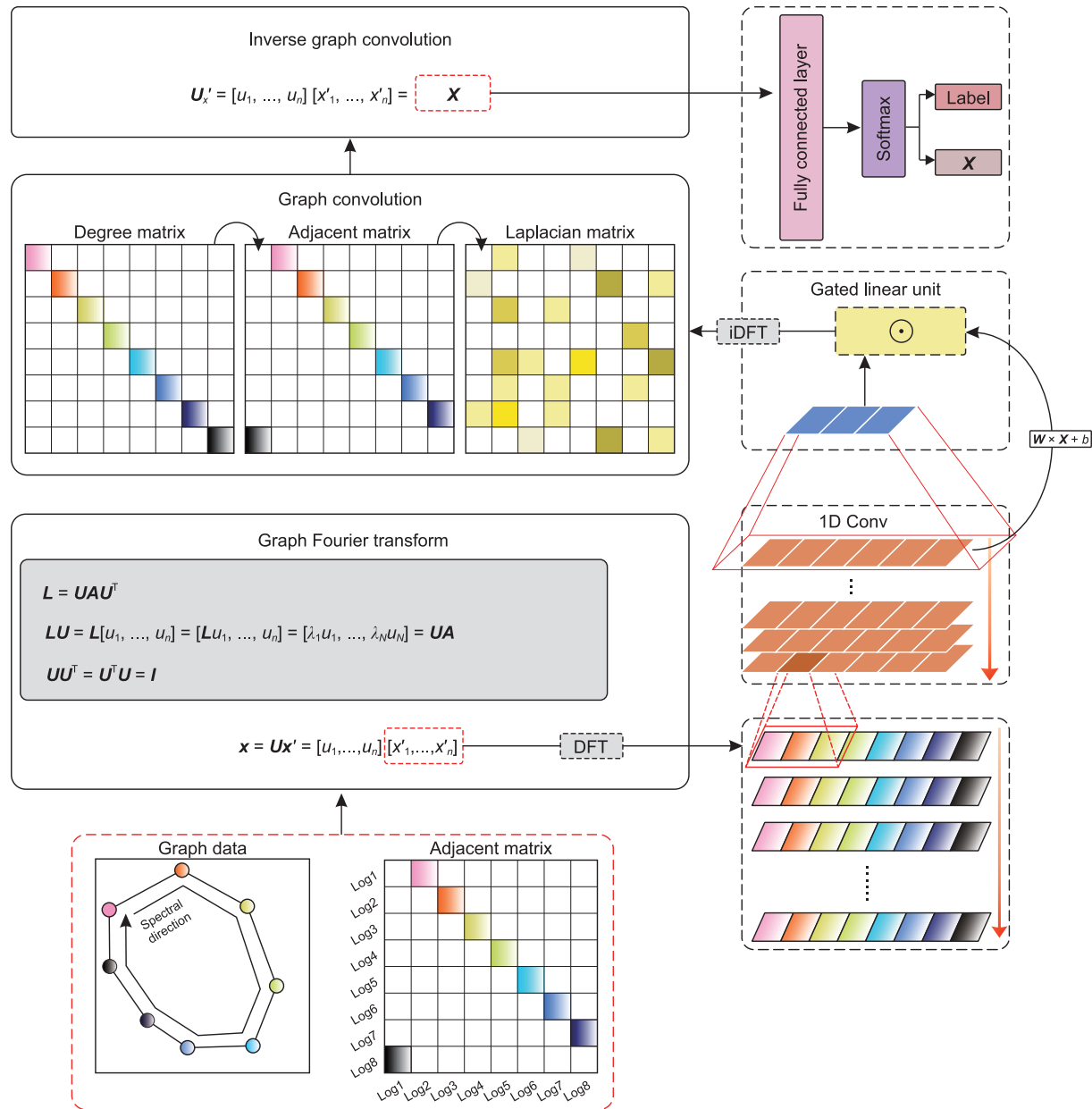


Fig. 8. Workflow of graph convolution network block.

$$\text{Loss}_{1\text{st}} = \text{MSE}(x_{\text{in}}, x) = \frac{1}{N} \sum_{i=1}^N (X - X_{\text{in}})^2 \quad (13)$$

The second part is the classification loss between the predicted probability distributions of labels ( $e^{\text{label}\sim}$ ) and the actual category labels ( $e^{\text{label}}$ ), defined as

$$\text{Loss}_{2\text{nd}} = \text{cross\_entropy}(\text{label}, \text{label}\sim) = -\log\left(\frac{e^{\text{label}}}{\sum e^{\text{label}\sim}}\right) \quad (14)$$

The overall loss is

$$\text{Loss} = \frac{1}{N} \sum_{i=1}^N (X - X_{\text{in}})^2 - \log\left(\frac{e^{\text{label}}}{\sum e^{\text{label}\sim}}\right) \quad (15)$$

To ensure the accuracy of machine learning models and prevent overfitting, we divided the dataset into training (60%, 7540), validation (30%, 3370), and test sets (10%, 1657). To compare the performance of different models, we selected prevalent evaluation metrics including accuracy, precision, recall, F1-score, and Area Under the ROC Curve (AUC).

Accuracy measures how often the model correctly predicts the actual label of a data point. It is calculated as the ratio of the number of correct predictions to the total number of predictions. A high accuracy indicates the model's strong ability to predict true labels correctly. However, accuracy alone can be misleading if there is a class imbalance in the dataset.

Precision measures the proportion of positive predictions made by the model that are actually correct. It is calculated as the ratio of true positives divided by all positive predictions (including false positives). High precision indicates a low false positive rate. However, optimizing for precision alone may result in a low recall.

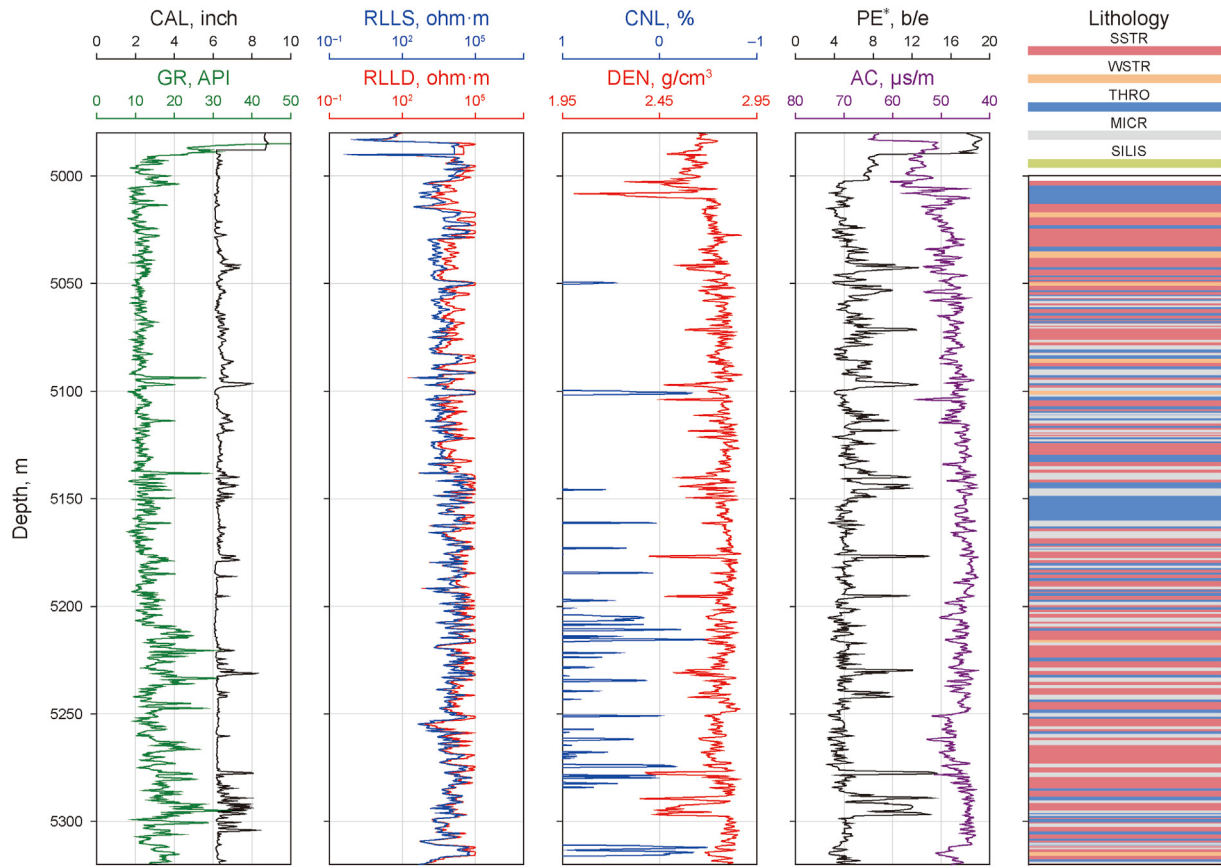


**Fig. 9.** Logging data and lithological analysis column of Moxi 9, Moxi gas field, central Sichuan Basin.

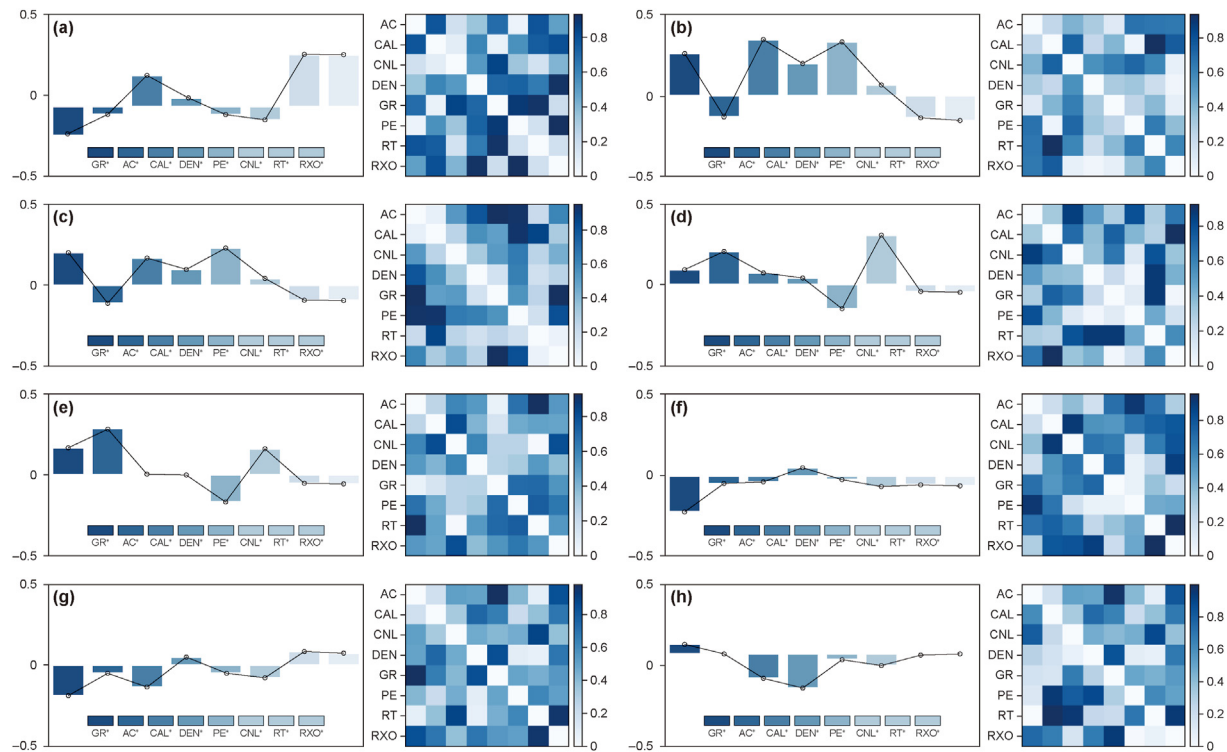


**Fig. 10.** Visualization of spectra (left part in each sub-figure) and graph (right part in each sub-figure) from Moxi 9, Moxi gas field, central Sichuan Basin (\* denotes the normalization of logging data). **(a)** 5308.08 m, SSTR; **(b)** 5300.06 m, WSTR; **(c)** 5224.68 m, WSTR; **(d)** 5210.53 m, THRO; **(e)** 5115.68 m, MICR; **(f)** 5045.75 m, SILIS; **(g)** 5035.92 m, SSTR; **(h)** 5013.27 m, THRO.

Recall measures the proportion of actual positive cases that are correctly predicted by the model. It is calculated as the ratio of true positives divided by the sum of true positives and false negatives. High recall indicates a low false negative rate. However, recall alone does not consider false positives.

F1-score balances both precision and recall by taking their harmonic mean. It captures both false positives and false negatives. A model with a high F1-score has both high precision and high recall.

The analysis metrics (Eqs. (16)–(20)) include *TP* for true positive predicted samples, *TN* for true negative predicted samples, *FP* for false positive predicted samples, and *FN* for false negative predicted samples. Score values range from 0 to 1, with higher values indicating better model performance.

$$\text{Accuracy} = \frac{TP + TN}{TP + TN + FP + FN} \quad (16)$$

$$\text{Precision} = \frac{TP}{TP + FP} \quad (17)$$

$$\text{Recall} = \frac{TP}{TP + FN} \quad (18)$$

$$\text{F1-score} = \frac{2TP}{2TP + FP + FN} \quad (19)$$

$$\text{AUC} = \int_0^1 \frac{TP}{TP + FN} \times \frac{FP}{TN + FP} d\left(\frac{FP}{TN + FP}\right) \quad (20)$$

## 4. Results

### 4.1. Latent graphs

In graph machine learning, the latent graphs include spectra and adjacent matrices. To illustrate the generation of latent graphs, several logging data is visualized from Moxi 9 (Fig. 9). All curves are normalized and annotated with an asterisk (\*). Fig. 10 displays a time-series spectrum (the left part in each sub-figure of Fig. 10) and the corresponding adjacent matrices graphs (the right part in each sub-figure of Fig. 10). Spectra with distinct shapes indicate different graph representations (Fig. 10). Spectra from same lithological labels display similar shapes (Fig. 10(b) and (c)) while the similar geometric features in the spectra would not reflect the same lithology (Fig. 10(d) and (e)). The complex projections between logging data and lithological labels is more flexible than traditional lithological interpretations by fixed logging plates. The visualized adjacent matrices are completely different (Fig. 10). The complexity of the adjacency matrix directly reflects that the graph data structure has better information entropy and information gain when characterizing logging data. With latent graphs, relations of different types of well logs are constructed, digging up the latent information from well logs and boosting the storage of latent information instead of training from data directly.

### 4.2. GCN model

The optimal GCN model was obtained after training 1200 epochs (Fig. 11). The hyper-parameters of the GCN model are shown Table 2. The results are shown in Fig. 12(a). The accuracy, precision, recall of training datasets are 0.98, 0.97 and 0.97. The F1-score is

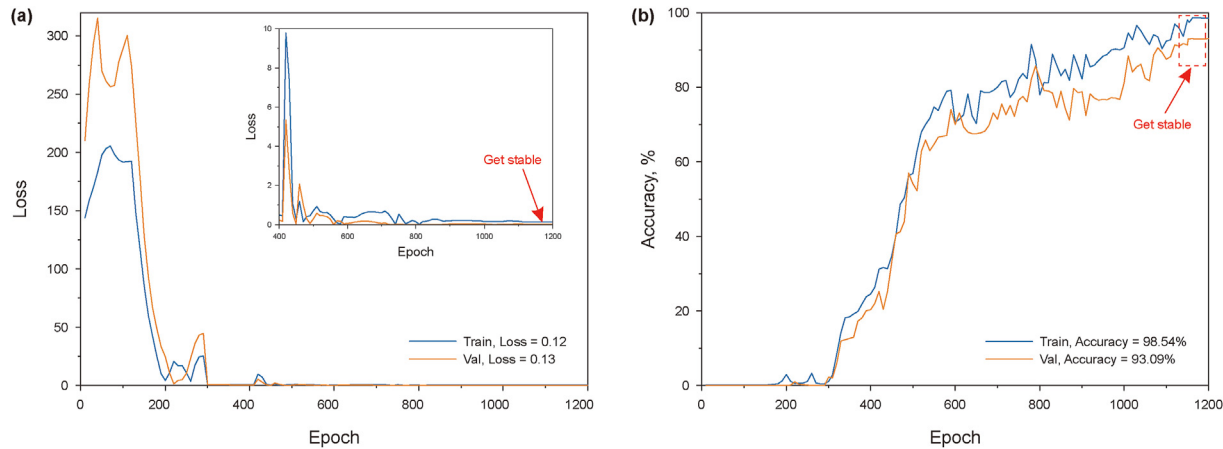


**Fig. 11.** Training performance of GNN (get stable means the model optimization stopped). **(a)** Loss variation with training datasets and test datasets (the sub-figure is the zoom loss variation of epoch 400 to 1200); **(b)** Accuracy variation with training datasets and test datasets.

**Table 2**  
The hyperparameters of different models.

Models	Best hyperparameters					
	Window	Epoch	Learning rate	Batch size	Dropout rate	Layer numbers
Min	2	600	1e-4	16	0	2
Max	9	1600	9e-2	128	0.6	10
GCN	3	1200	5e-4	32	0.4	—
LSTM	—	1300	5e-4	64	0.3	5
RNN	—	1200	1e-4	32	0.3	5
ANN	—	1200	1e-4	32	0.3	6

When the dropout rate is 0, the CNN model becomes FCNN model.

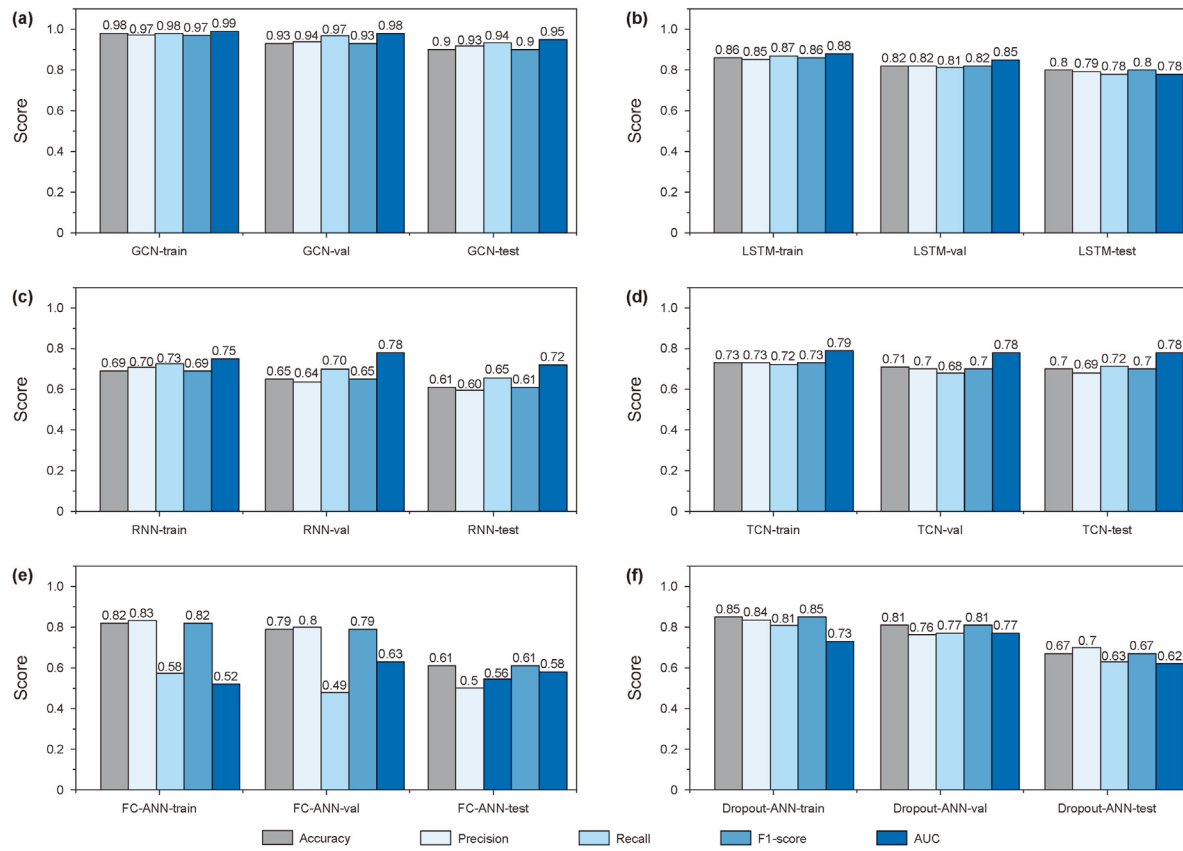


**Fig. 12.** Performance of time-series-based models and data-shuffled models. **(a)** GCN; **(b)** LSTM; **(c)** RNN; **(d)** TCN; **(e)** FC-ANN; **(f)** Dropout-ANN.

0.97 and the AUC is 0.93. The respective measurements for validation datasets are 0.93, 0.94, 0.97, 0.93, and 0.98. The respective measurements for test datasets are 0.9, 0.93, 0.94, 0.9, and 0.95.

#### 4.3. LSTM model

Long short-term memory (LSTM) is a model to handle the long time-series sequence data. The results are shown in Fig. 12(b). The top-performing LSTM model achieves accuracy, precision, recall, F1-score and AUC values of 0.86, 0.85, 0.87, 0.86 and 0.88, respectively, on the training datasets. The validation datasets yield measurements of 0.82, 0.82, 0.81, 0.82 and 0.85 for accuracy, precision, recall, F1-score and AUC, respectively. The test datasets produce measurements of 0.8, 0.79, 0.78, 0.8 and 0.78 for accuracy, precision, recall, F1-score and AUC, respectively. The hyper-parameters of the LSTM model are shown Table 2.

#### 4.4. RNN model

The architecture of recurrent neural network (RNN) is similar to that of the LSTM model. RNN is considered a fundamental model for processing short time-series data. The results are shown in Fig. 12(c). The respective measurements for the training datasets are 0.69, 0.7, 0.73, 0.69 and 0.75. The respective measurements for the validation datasets are 0.65, 0.64, 0.7, 0.65 and 0.78. The respective measurements for the test datasets are 0.61, 0.6, 0.65, 0.61 and 0.72. The hyper-parameters of the RNN model are shown Table 2.

#### 4.5. TCN model

The temporal convolutional network (TCN) shares similar architecture with LSTM and RNN. The TCN utilizes convolution kernels for time series extraction. The results are shown in Fig. 12(d). The training datasets yield measurements of 0.73, 0.73, 0.72, 0.73 and 0.79. The validation datasets yield measurements of 0.71, 0.7, 0.68, 0.7 and 0.78. The test datasets yield measurements of 0.7, 0.69, 0.72, 0.7 and 0.78. The hyper-parameters of the TCN model are shown Table 2.

#### 4.6. FC-ANN and Dropout-ANN

The artificial neural network (ANN) is an effective model that has been successfully implemented in logging interpretation. Dropout is a commonly used technique in neural networks to mitigate overfitting.

The fully connected artificial neural network (FC-ANN) achieves respective accuracy, precision, recall, F1-score and AUC of 0.82, 0.83, 0.58, 0.82 and 0.52 in the training datasets. The respective measurements for the validation datasets are 0.79, 0.8, 0.49, 0.79 and 0.63. The respective measurements for the test datasets are 0.61, 0.5, 0.56, 0.61 and 0.58. The results are shown in Fig. 12(e).

The local dropout connected artificial neural network (Dropout-ANN) achieves respective accuracy, precision, recall, F1-score and AUC of 0.85, 0.84, 0.81, 0.85 and 0.73 in the training datasets. The respective measurements for the validation datasets are 0.81, 0.76, 0.77, 0.81 and 0.77. The respective measurements for the test datasets are 0.67, 0.7, 0.63, 0.67 and 0.62. The hyper-parameters of the FC and Dropout-ANN models are shown Table 2. The results are shown in Fig. 12(f).

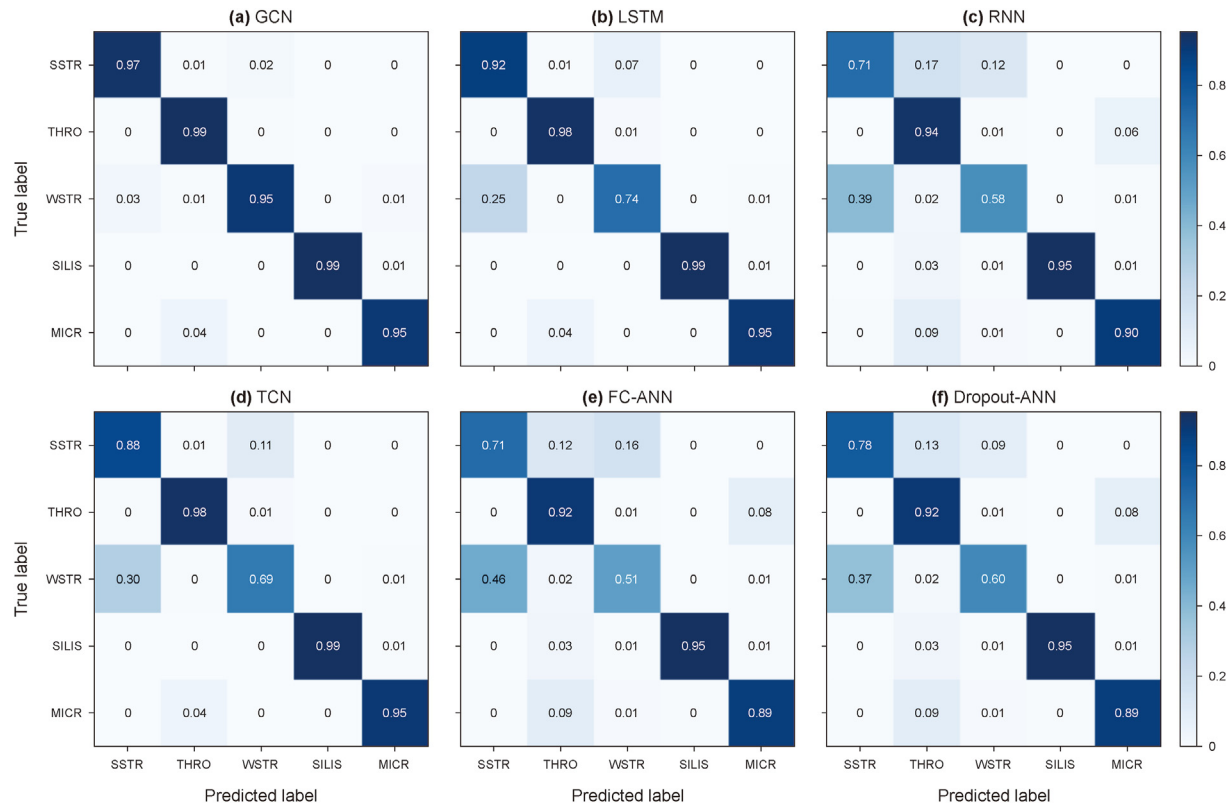


**Fig. 13.** Confusion matrixes of time-series-based models and data-shuffled models. **(a)** Confusion matrix of GNN; **(b)** confusion matrix of LSTM; **(c)** confusion matrix of RNN; **(d)** confusion matrix of TCN; **(e)** confusion matrix of FC-ANN; **(f)** confusion matrix of Dropout-ANN.

**Table 3**

The performances of models with the only GR input (all models reach SOTA).

Best model	The performance in the preserved datasets				
	Acc	Pre	Recall	F1	AUC
LSTM-sequential	0.44	0.43	0.44	0.44	0.55
RNN-sequential	0.39	0.37	0.36	0.38	0.40
TCN-sequential	0.41	0.40	0.41	0.40	0.43
FC-ANN-sequential	0.22	0.20	0.21	0.22	0.19
Dropout-ANN-sequential	0.25	0.22	0.23	0.24	0.20
LSTM-unsequential	0.23	0.21	0.22	0.23	0.20
RNN-unsequential	0.19	0.19	0.19	0.20	0.19
TCN-unsequential	0.20	0.20	0.20	0.20	0.20
FC-ANN-unsequential	0.22	0.19	0.21	0.22	0.21
Dropout-ANN-unsequential	0.24	0.22	0.23	0.24	0.21

Note: Acc = Accuracy, Pre = Precision; F1=F1-score.

## 5. Discussion

### 5.1. Models comparison

#### 5.1.1. Multi-dimensional indexes comparison

Fig. 12 shows the GCN model demonstrates superior prediction ability compared to other models (Fig. 12). While FC-ANN and Dropout-ANN achieve high accuracy in training and validation datasets, their evaluating metrics drop significantly in the test datasets ( $\Delta$ Accuracy = 0.21,  $\Delta$ Precision = 0.33,  $\Delta$ F1-score = 0.21, Fig. 12(e)). This indicates overfitting of the ANN models, where they perform well on the training data but struggle with unseen data. Previous research has shown that dropout strategy is effective in reducing overfitting (Wager et al., 2013; Srivastava et al., 2014; Pham et al., 2014; Xiao et al., 2016). In this study, a slightly improved dropout method leads to almost 20% improvement in all

**Table 4**

The pseudocode of Bayesian–statistic algorithm.

#### Algorithm Bayesian–statistic ( $L, d, i, k, l, P$ )

```

Input: Lithology column L ( $d, i, l$ )
      Depth  $d$ 
      Depth point  $i, (i+1)–(i) = 0.125$  m
      Lithology of microbialite  $l$ 
      Moving window  $k$ 
      Probability  $P$ 
Output: Estimate of the conditional probability from Walther's law via window moving
1: Initialization:  $L = \{l_1, l_2, l_3, \dots, l_d\}$ 
2: Initialization:  $P$ 
3: for count = 0 to int( $d/k$ ) do
4:   for each  $k$  do
5:     Num ( $P_{l/l_i}$ ) = Num ( $l_{i+1}|l_i$ )
6:   end for
7: end for

```

metrics in the whole datasets (Fig. 12(f)). However, with shuffling and destroying the time-series information, the ANN models performed poorly in microbialite classification. This result reveals the time-series information boosted the performance of automatic models.

LSTM models, known for handling long time-series sequences (Graves, 2012; Srivastava et al., 2015), outperform RNN models, which are better suited for short time-series sequences (Lipton, 2015). The LSTM models achieve higher evaluating metrics than RNN models (0.8, 0.79, 0.78, 0.8 and 0.78 vs. 0.61, 0.60, 0.65, 0.61 and 0.72, in the test datasets, Fig. 12(b) and (c)), indicating the LSTM model has stronger suitability for capturing time-series information in data-logging processing. On the other hand, the time-series information in the well-logging data is close to the long time-series

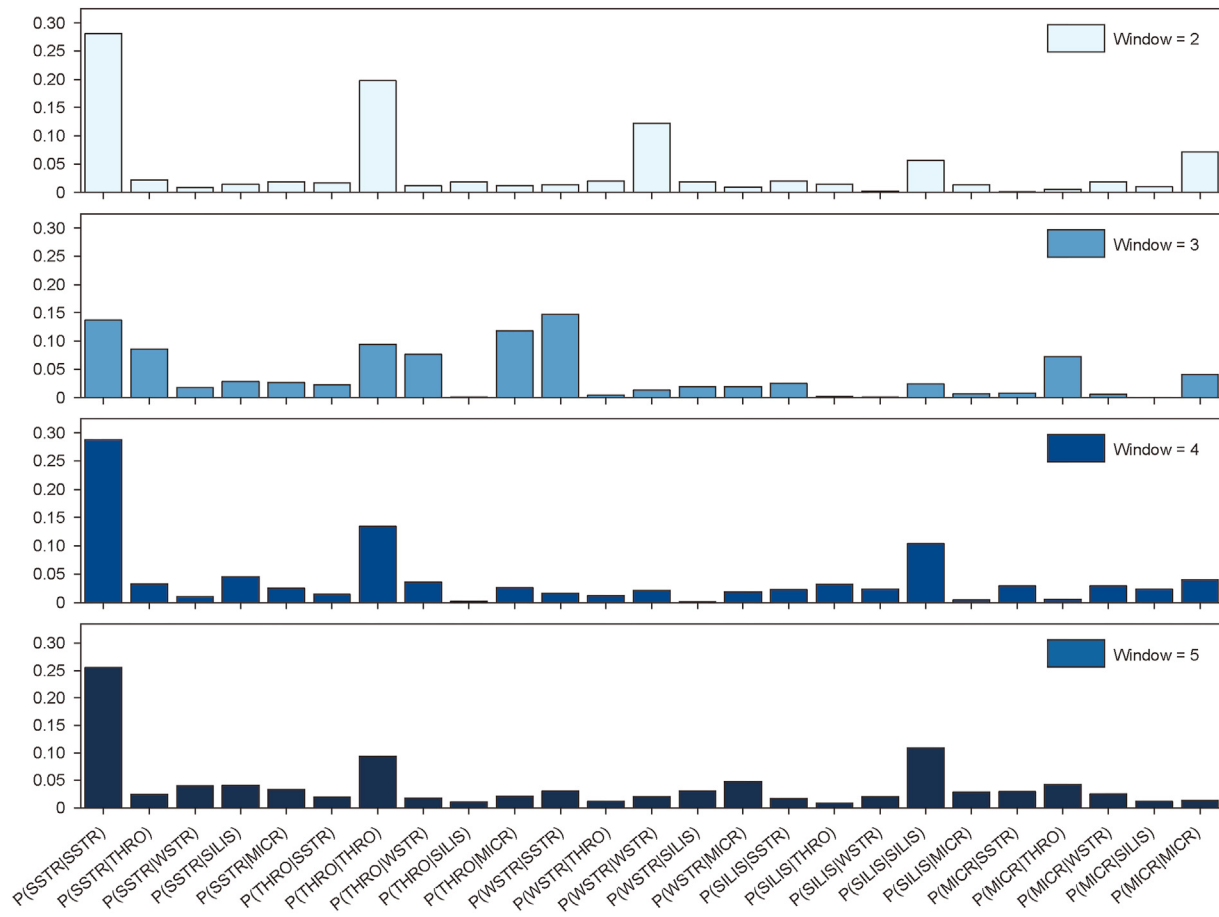


**Fig. 14.** Results of the statistics to detect the lithology change. (a) Window size = 2; (b) window size = 3; (c) window size = 4; (d) window size = 5.

information. Although theoretically TCN models are expected to perform better in time-series modeling tasks (Bai et al., 2018), in this study, their metrics surpasses RNN models but falls short of LSTM models. This discrepancy may be due to the TCN model's super-long receptive field, which exceeds the typical scale of deposit fluctuation for microbialite. This result proves the type of time-series information in the well-logging data is the long time-series information but not the super-long type. The length of time-series is possibly controlled by the deposition length.

In addition, expect for time-series modeling, another distinction between the GCN model and the time-series models (LSTM, RNN and TCN models) is the spectra, which models the latent information of binary well logs. The equal and high metrics in the GCN suggests the latent information among well logs is another method to improve model's performance (Fig. 12(a), (b), (c), (d)).

#### 5.1.2. Generalization test comparison

The generalizability of machine learning models to new data (two preserved wells,  $n = 284$ ) is another critical aspect in evaluating model performance. To simulate real-world well-logging interpretation, we utilized untrained logging-label paired data to test the models' ability to make predictions on unseen data. In practical exploration, understanding the specific types of misclassifications made by a model can provide more actionable insights than summary evaluation metrics alone. We visualized the models' confusion matrices on untrained datasets (Fig. 13) to reveal the distribution of prediction errors across microbialite classes. The graph convolutional network (GCN) model demonstrated superior

generalization capabilities, with test accuracies exceeding 0.95 for all microbialite types (Fig. 13(a)).

The long short-term memory (LSTM) model demonstrated excellent ability in identifying thrombolite (THRO), siliceous stromatolite (SILIS), and dolomiticrite (MICR), with accuracies exceeding 0.95 for each class (Fig. 13(b)). However, the LSTM model showed limitations in distinguishing between wavy stromatolites (WSTR) and stratiform stromatolites (SSTR). 25% of WSTR samples were misclassified as SSTR by the LSTM model (Fig. 13(b)). For SSTR samples, 7% were incorrectly predicted as WSTR (Fig. 13(b)).

The recurrent neural network (RNN) model exhibited similar performance to the LSTM, with slightly reduced accuracy on THRO (0.94), SILIS (0.95), and MICR (0.90) (Fig. 13(c)). The RNN model performed worse at predicting SSTR (0.71) and WSTR (0.58) (Fig. 13(c)) compared to the LSTM (Fig. 13(b)). 17% and 12% of SSTR samples were misclassified by the RNN as THRO and WSTR, respectively, while 39% of WSTR samples were incorrectly classified as SSTR (Fig. 13(c)).

The temporal convolutional network (TCN) model matched the LSTM model's accuracy on THRO, SILIS, and MICR prediction (Fig. 13(d)). However, the TCN demonstrated similar difficulties as the LSTM and RNN models in distinguishing between SSTR and WSTR (Fig. 13(d)). 11% of SSTR samples were mispredicted as WSTR by the TCN, while 46% of WSTR samples were mistakenly identified as SSTR (Fig. 13(d)), indicating poorer delineation of these two classes compared to the other models.

For the fully connected and dropout artificial neural network (ANN) models, performance on THRO, SILIS, and MICR prediction

was comparable (0.92, 0.95, and 0.89, respectively, Fig. 13(e)). The Dropout-ANN model demonstrated improved identification of SSTR (0.78) and WSTR (0.60) versus the FC-ANN model (0.71 and 0.51, respectively, Fig. 13(f)).

Visualizing and comparing the confusion matrices highlights the relative strengths and weaknesses of each model architecture at predicting specific microbialite classes from the unlabeled test data. In summary, for microbialite interpretation, the challenge is separating the WSTR and SSTR. With the assistance of time-series modeling, the performance of distinguishing WSTR and SSTR would be boosted. By introducing additional latent information among logs, the GCN would improve the capability of separating the two closing types.

### 5.2. Importance and analysis of the time-series

The machine learning models can be categorized into three groups based on the data representations used. The graph convolutional network (GCN) model incorporates both time-series and spectral information from the well logs. The long short-term memory (LSTM), recurrent neural network (RNN), and temporal convolutional network (TCN) models solely utilize time-series data. Finally, the fully-connected and dropout artificial neural network (ANN) models do not explicitly encode time-series or spectral data.

Across training, validation, test, and hold-out datasets, the GCN model achieved superior performance for microbialite classification. The LSTM and TCN models also demonstrated acceptable predictive capabilities, with sequential models showing an advantage over non-sequential architectures. To isolate the impact of time-series information, we performed an experiment using only the GR log as input, precluding construction of the latent graph structure. In this setting, we compared the LSTM, RNN, and TCN models versus the FC-ANN and Dropout-ANN models.

The accuracy, precision, recall, F1-score, and AUC metrics (Table 3) indicate that time-series models (LSTM, RNN, TCN) significantly outperformed the non-sequential ANN models given GR log input alone (Table 3). To further analyze the importance of temporal ordering, we evaluated models on shuffled GR data with randomized time steps. On shuffled data, all metrics of the LSTM, RNN, and TCN models decreased substantially to the level of the ANN models, which showed little change in performance (Table 3). The degraded time-series model performance on shuffled data demonstrates that temporal ordering of the logs provides critical information for lithological prediction.

To examine the relationship between time-series structure and lithological transitions, we implemented a Bayesian statistical algorithm (pseudocode in Table 4) that models the sedimentary sequence as a Markov process.

At a window of 2 (0.25 m), transitions between the same lithology dominated (Fig. 14(a)). At a window of 3 (0.375 m), transitions between different microbialites became apparent (Fig. 14(b)), suggesting this captures an appropriate scale for lithological cycles. Larger windows (0.5, 0.625 m) again showed self-transitions dominating (Fig. 14(c) and (d)). The detected peak transition probability scale of 3 matches the GCN model's window size. Overall, these statistical results support incorporating time-series data to model lithological sequences. The superior performance of time-series models coupled with the detected lithological transitions validate that time-series information from well logs enhances microbialite classification.

### 5.3. Importance and analysis of the spectra

The spectral representations in the GCN model provide another potential improvement over standard machine learning approach. To

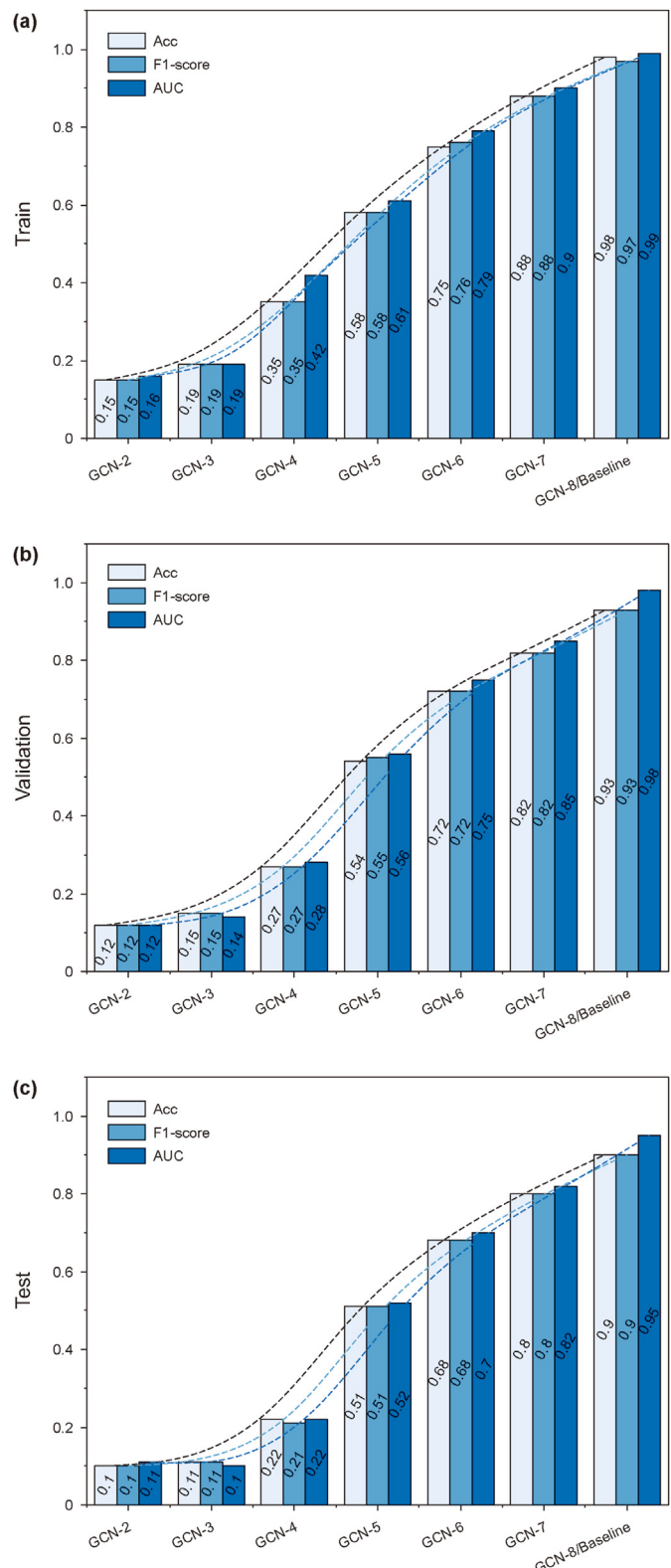


**Fig. 15.** Performance variations among the number of logs in different datasets. (a) Train datasets; (b) validation datasets; (c) test datasets.

evaluate the influence of spectral length and logging types, as well as discuss the importance of spectra for lithological prediction, we trained a series of GCN models with different input data configurations. The accuracy, precision, recall, F1-score, and AUC metrics were

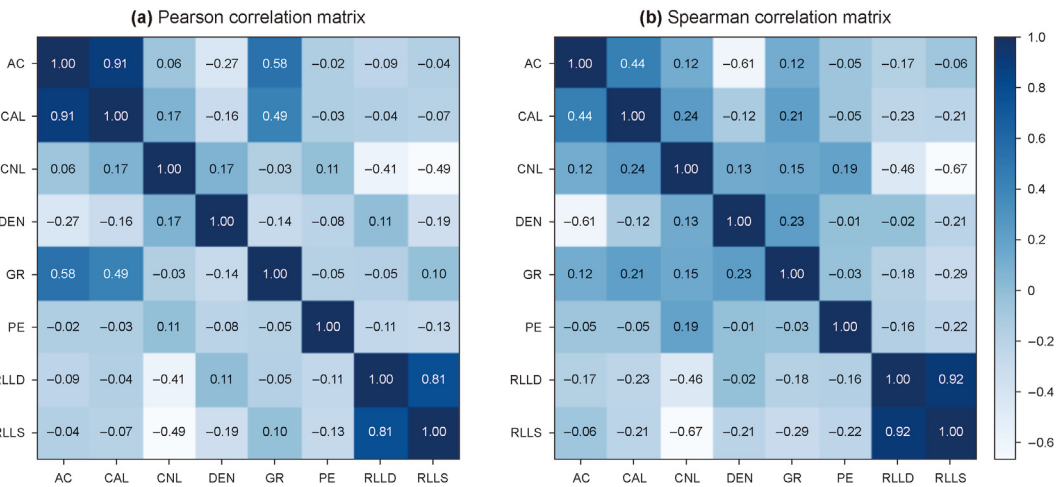


**Fig. 16.** The correlation matrices of well logs. **(a)** Pearson correlation matrix; **(b)** Spearman correlation matrix.

**Table 5**

The results of ablation experiments (in the test datasets, all models reach SOTA).

Ablations	Performance				
	Accuracy	Precision	Recall	F1-score	AUC
GCN (baseline)	0.90	0.93	0.94	0.90	0.95
w/o GRU	0.72(−0.22)	0.71(−0.22)	0.73(−0.21)	0.72(−0.18)	0.70(−0.25)
w/o Attention	0.84(−0.06)	0.80(−0.13)	0.82(−0.12)	0.84(−0.06)	0.86(−0.09)
w/o DFT	0.82(−0.08)	0.81(−0.12)	0.82(−0.12)	0.82(−0.18)	0.73(−0.22)
w/o GFT	0.80(−0.10)	0.81(−0.12)	0.80(−0.14)	0.80(−0.10)	0.79(−0.16)
w/o Convolution	0.62(−0.28)	0.59(−0.34)	0.61(−0.33)	0.61(−0.29)	0.48(−0.47)
Add 1 GNN	0.89(−0.01)	0.88(−0.05)	0.89(−0.05)	0.90(0.00)	0.95(0.00)
w/o GNN 1	0.82(−0.08)	0.80(−0.13)	0.81(−0.13)	0.82(−0.08)	0.81(−0.14)
w/o GNN 2	0.83(−0.07)	0.82(−0.11)	0.80(−0.14)	0.83(−0.07)	0.81(−0.14)

Note: w/o means without.

averaged across combinations of logging data types for the training, validation, and test sets. For example, GCN-2 indicates GCN models trained on two logging data types. Averaging aims to reduce the influence of differences between logging type combinations.

Across all datasets, model performance improved with the inclusion of additional logging data to construct longer spectra (Fig. 15). These results suggest the length of the spectral representation positively influences GCN model capabilities. To analyze relationships between logs and assess the value of constructing spectra, we computed Pearson (Fig. 16(a)) and Spearman correlation matrices (Fig. 16(b)). The RLLD and RLLS logs exhibit high correlation in both matrices. In standard machine learning, one of these redundant logs would often be discarded. However, dropping either RLLD or RLLS resulted in decreased accuracy, precision, recall, F1-score, and AUC of 0.85, 0.84, 0.84, 0.85, 0.86 and 0.82, 0.83, 0.81, 0.82, 0.84, respectively (in the test datasets, in contrast with the performance of 0.9, 0.93, 0.94, 0.9 and 0.95, Fig. 12(a)). This indicates the highly correlated logs provide additional latent information to the GCN models.

The Pearson and Spearman matrices show RLLD and RLLS have similar but distinct correlations to other logs. Specifically, RLLD logs are more negatively correlated across features (Fig. 16). This complementary correlation, alongside the performance drop when excluding either log, suggests the spectral boost stems not from redundancy but rather from extracting complex latent signals. Overall, constructing spectra from multiple logs, even if correlated, allows the GCN model to learn richer representations for improved lithological prediction.

#### 5.4. Ablation experiments for GCN

Ablation experiments were conducted to evaluate the effects of different components within the GCN model architecture. Removing the GRU results in building graphs directly from raw logging data without any time series feature extraction. This caused accuracy, precision, recall, F1-score, and AUC to drop substantially to 0.72, 0.71, 0.73, 0.72, and 0.70, decreasing by 0.18, 0.19, 0.21, 0.18, and 0.25, respectively (Table 5). These significant declines indicate the graph construction process is critical for the GCN model.

Eliminating the self-attention mechanism leads to smaller decreases in performance of 0.06, 0.13, 0.12, 0.06, and 0.09 for the three metrics (Table 5), suggesting self-attention provides moderate improvements. Similarly, excluding the DFT and GFT blocks results in slight drops in accuracy, precision, recall, F1-score, and AUC (Table 5), demonstrating the value of graph Fourier transforms in the GCN.

The most drastic declines occurred when removing convolution operations, which lowered accuracy, precision, recall, F1-score, and AUC to 0.62, 0.59, 0.61, 0.61, and 0.48, reducing them by 0.28, 0.34, 0.33, 0.29, and 0.47, respectively (Table 5). These substantial decreases highlight convolution as one of the most vital operations within the GCN model. Modifying the number of GNN blocks shows limited effects on overall performance. The architecture with two GNN blocks appears optimal for microbialite identification.

In summary, the ablation study quantitatively analyzes the contribution of each component to the GCN model capabilities. The time series feature extraction, graph construction, Fourier transforms, and convolutions are all critical for effective lithological

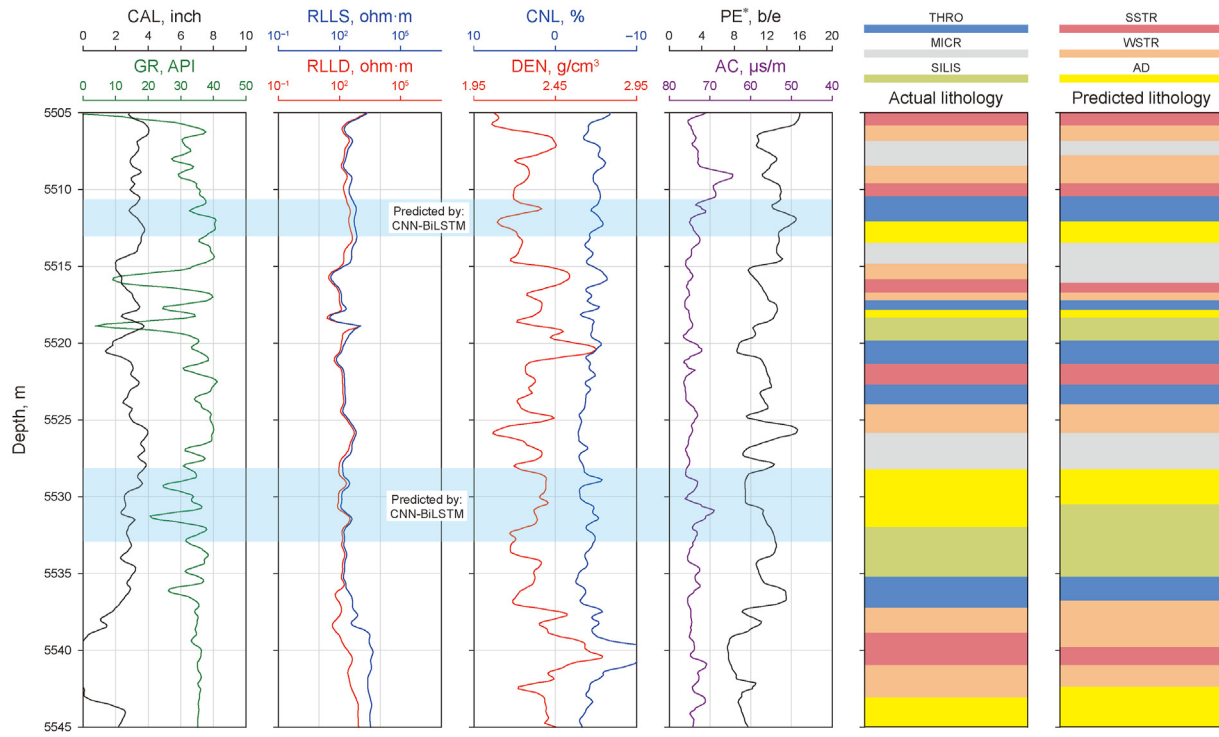


**Fig. 17.** Logging data, lithological analysis column and predicting lithological column of the Dengying-2, Taihe gas field, North slope of central Sichuan basin, X well (The actual lithological labels were obtained by core analysis and microscopic verification).

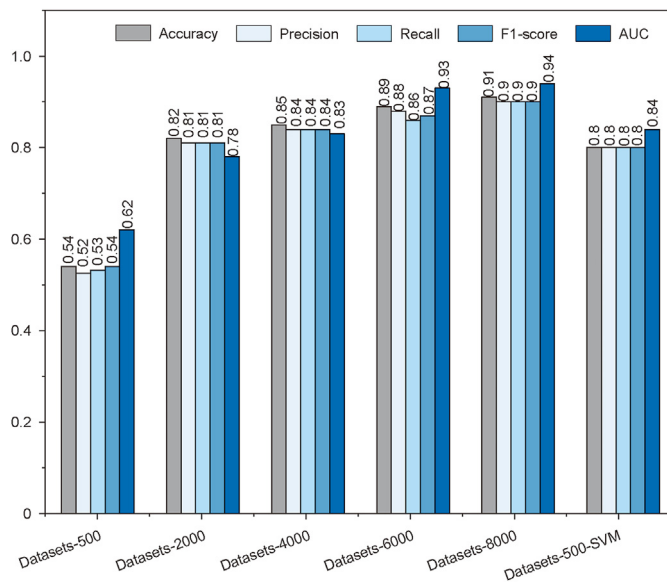


**Fig. 18.** The performances of the fine-tune GCN models with different data and strategy.

prediction from well log data.

### 5.5. Applications in other strata

Previous machine learning research has given limited attention to applications in petroleum exploration. Existing trained models are constrained to individual strata or depositing areas, restricting their utility. To demonstrate how pretrained models can overcome real-world challenges, we present two examples of applying such

models in practice. The primary strategy for leveraging pretrained networks on new target formations is via fine-tuning.

Fine-tuning involves initializing a model with weights from training on a source domain, then continuing training on data from the target domain of interest. This transfer learning approach allows models to adapt to new tasks and distributions without requiring full retraining. Fine-tuning pretrained models enables exploiting knowledge from source domains to accelerate convergence and improve generalization on target tasks with limited data.

Here, we showcase fine-tuning for two scenarios: extending pretrained lithology prediction models to new geological areas and formations. In both cases, models trained on well log data from one region or stratum are fine-tuned on small target datasets. Fine-tuning rapidly optimizes model weights to combine generalization from the initial training with target-specific adaptation. These demonstrations highlight the potential for transfer learning to unlock the value of pretrained models across diverse subsurface settings. Overall, fine-tuning provides a practical solution to tailor off-the-shelf machine learning for cost-effective application in new petroleum exploration initiatives.

#### 5.5.1. The second member of the Dengying Formation

The second member of the Dengying Formation (Dengying-2) contains similar logging data to Dengying-4 in the Moxi gas field. We collected 8473 samples from Dengying-2 in the Taihe Gas Field (Fig. 1(a), THG, NS), including wackestone, boundstone, thrombolite, silicified microbialite, micrite, and a new lithology-spongiosstromata boundstone. Missing logs were generated via a semi-supervised convolutional neural networks (CNN) and bidirectional long-short term memory networks (BiLSTM) (CNN-BiLSTM, Fig. 17, shadow part). To study the impact of dataset size, samples were split into subsets of 500–8000 data points (Fig. 18). The 500-sample set simulates limited logging data where overfitting readily occurs during training.

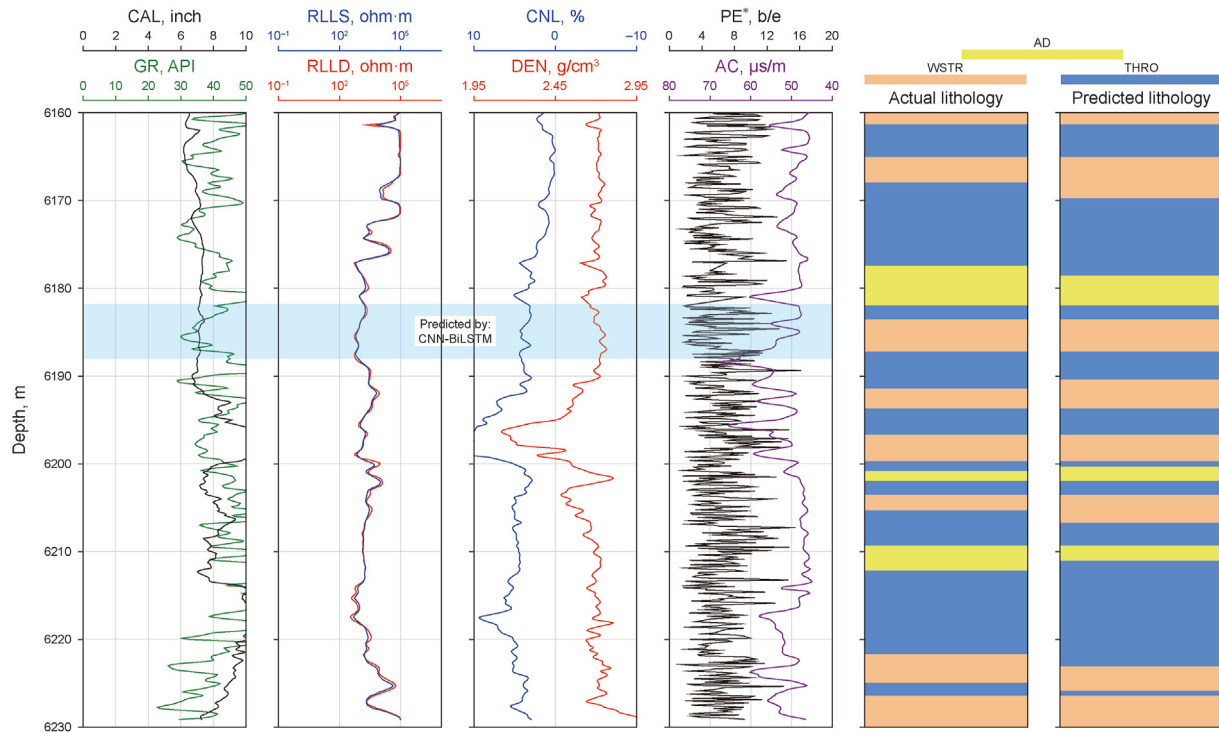


**Fig. 19.** Logging data, lithological analysis column and predicting lithological column of the Triassic Leikoupo-43, Pengzhou gas field, west Sichuan Basin, X well (The actual lithological labels were obtained by core analysis and microscopic verification).

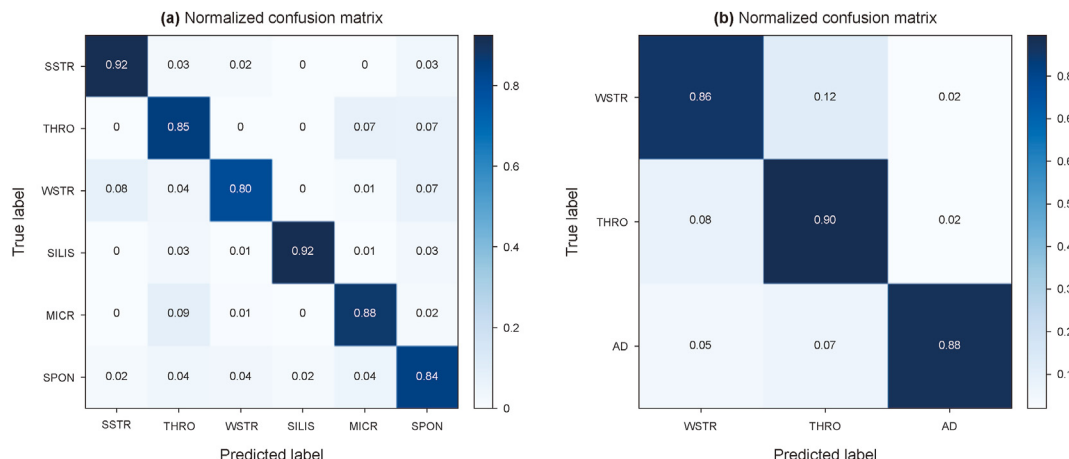


**Fig. 20.** The confusion matrix of the fine-tune GNN model. (a) Fourth member of Dengying Formation, Taihe Gas field, North slope of central Sichuan basin; (b) Leikoupo-4<sup>3</sup>, Pengzhou gas field, west Sichuan basin.

Results demonstrate fine-tuning performance improves as more training data is utilized (Fig. 18). With only 500 samples, accuracy, precision, recall, F1-score, and AUC of the fine-tuned model dropped compared to training on larger sets (Fig. 18). 500-sample training and validation accuracy were 0.86 and 0.64 respectively, indicating overfitting. To enable effective fine-tuning, a two-step approach was adopted – the pretrained model extracted features, then multiple support vector machine (SVM) classifiers were trained on the features. This boosted performance for the 500-sample case (Fig. 18). With the full 8000 samples, exceeding 80% samples can be right predicted (Fig. 20(a)).

In summary, sufficient training data is crucial to realize the full benefits of fine-tuning for lithology prediction. When data is

limited, supplementing fine-tuned models with classifiers like SVM can improve generalization. Overall, this study demonstrates how transfer learning strategies can adapt pretrained models to new formations given modest target domain data.

#### 5.5.2. The third submember of the fourth member of the Leikoupo Formation

The fourth member of the Leikoupo Formation (Leikoupo-4), deposited during the late Triassic, contains abundant microbial sediments including wackestone, thrombolite, and algal dolarenite. Due to mineralogical variations from different depositional environments, models trained on the fourth member of the Dengying Formation cannot be directly applied to Leikoupo-4. Developing

accurate lithology prediction rapidly is essential yet challenging in practice. Fine-tuning provides a widely adopted strategy in computer vision to adapt pretrained models.

We demonstrate fine-tuning on Leikoupo-4 with a model pre-trained on Dengying Formation data. Over 2000 samples were collected from the third submember of Leikoupo-4 (Leikoupo-43) in the Pengzhou gas field (Fig. 1(a)–PZG). The train: validation: test ratio was 6:3:1. Compared to the Dengying Formation, logging data from Leikoupo-43 lacks photoelectric (PE) curves (Fig. 19). Logs were also sparse. To input complete consistent data, missing logs were generated via a CNN-BiLSTM model (Fig. 19, shadow part).

Fine-tuning began by loading pretrained model hyperparameters and adjusting the output dimension from five (Dengying-4 lithologies) to three (Leikoupo-43 lithologies). The altered model was then trained on the Leikoupo-43 data. Accuracy, precision, recall, F1-score, and AUC on the train, validation, and test datasets were 0.84, 0.83, 0.85; 0.82, 0.81, 0.84; and 0.81, 0.81, 0.83, respectively. Exceeded 85% lithologies can be right predicted (Fig. 20(b)).

In summary, fine-tuning rapidly adapts a pretrained model to new formations and areas by retraining on small target datasets. This demonstration highlights the potential of transfer learning to unlock generalization capabilities from past training for cost-effective lithology prediction in practice.

## 6. Conclusion

In this study, various neural network models including Graph Convolutional Networks (GCN), Long-Short Term Memory (LSTM), Recurrent Neural Networks (RNN), Temporal Convolutional Networks (TCN), and two types of Artificial Neural Networks (ANNs) were evaluated for lithology prediction within the fourth member of Dengying Formation, Moxi gas field. Key findings include:

- (1) GCN performance: GCN emerged as the superior model, achieving high metrics in accuracy (0.90), precision (0.93), recall (0.94), F1-score (0.90), and AUC (0.95), with approximately 90% of samples correctly classified. Comparison with other models: LSTM, RNN, and TCN showed better performance over ANNs by utilizing sequential logging data, whereas ANNs exhibited overfitting issues. Misclassifications were primarily between stratiform and wavy stromatolites.
- (2) Relationships between time-series and sedimentary sequence: Time-series information boosted models' performance because of the better modeling of actual sedimentary depositing sequence.
- (3) Spectral and graph information utilization: Incorporation of spectral data and the graph data enhanced classification by identifying multi-log correlations and modeling the latent information.
- (4) Ablation study results: Essential to GCN's performance were its graph convolutional and gated recurrent unit layers for effectively processing graph and sequential data, which is more effective to find the length of sedimentary sequence.
- (5) Transfer Learning: GCN demonstrated excellent adaptability to new microbialite types with minimal additional training, showcasing potential for application across various formations. Even with a limited dataset (less than 500 samples), integrating GCN feature extraction with SVM classification yielded effective results.

In summary, leveraging graph data containing time-series and spectral information significantly enhances lithology prediction

capabilities. GCN stands out as a particularly promising model for the petroleum industry, offering efficient generalization to new domains through graph-structured data and transfer learning.

## CRediT authorship contribution statement

**Ke-Ran Li:** Writing – original draft, Data curation, Conceptualization. **Jin-Min Song:** Writing – review & editing, Resources, Funding acquisition, Conceptualization. **Han Wang:** Methodology, Investigation, Data curation. **Hai-Jun Yan:** Resources, Project administration. **Shu-Gen Liu:** Project administration, Funding acquisition, Conceptualization. **Yang Lan:** Software, Methodology, Data curation. **Xin Jin:** Validation, Methodology, Investigation. **Jia-Xin Ren:** Software, Investigation. **Ling-Li Zhao:** Formal analysis, Data curation. **Li-Zhou Tian:** Methodology, Investigation. **Hao-Shuang Deng:** Methodology, Data curation. **Wei Chen:** Resources, Investigation, Formal analysis.

## Declaration of competing interest

The authors declare that they have no known competing financial interests or personal relationships that could have appeared to influence the work reported in this paper.

## Acknowledgements

This study was supported by National Natural Science Foundation of China (Nos. 41872150, U2344209 and U19B6003) and the PetroChina Southwest Oil and Gasfield Company (No. 2020-54365).

## Nomenclature

GCNs	Graph convolution networks
GRUs	Gate Recurrent Units
LSTM	Long–short temporal memory models
RNNs	Recurrent neural networks
TCNs	Temporal convolution networks
ANNs	Artificial neural networks
FC-ANNs	fully Connected artificial neural networks
Dropout-ANNs	Artificial neural networks with dropout method
XGBoost	Extreme Gradient Boost
PINN	Physics-informed neural networks
CNN-BiLSTM	Convolution neural network combined with bi-direction LSTM model
SVM	Support vector machine
Z <sub>2</sub> dn	Dengying Formation
Z <sub>2</sub> dn <sub>1</sub>	First member of Dengying Formation
Z <sub>2</sub> dn <sub>4</sub>	Fourth member of Dengying Formation
MICR	Dolomiticrite
SSTR	Stratiform stromatolite
WSTR	Wavy stromatolite
THRO	Thrombolite
SILIS	Siliceous stromatolite
AC	Acoustic log
CAL	Caliper well log
CNL	Compensated neutron log
DEN	Density log
GR	Gamma-ray log
PE	Photoelectric absorption cross-section index log
RLLD	Deep lateral resistivity log
RLLS	Shallow resistivity log
SMOTE	Synthetic minority over-sampling technique
SOTA	State-of-the-art/best
TOC	Total organic carbon
CNNs	Convolution neural networks

DFT	Discrete Fourier transform
GLU	Gated linear unit
iDFT	Inverse discrete Fourier transform
e <sub>label</sub>	Predicted probability distributions of labels
e <sub>label</sub>	Actual category labels
ROC	Receiver Operating Characteristic
AUC	Area Under the ROC Curve
TP	Number of true positive predicted samples
TN	Number of true negative predicted samples
FP	Number of false positive predicted samples
FN	Number of false negative predicted samples
*	Normalized logging data
Dengying-2	Second member of the Dengying Formation
Dengying-4	Fourth member of the Dengying Formation
THG	Taihe gas field
NS	North slope
Leikoupo-4	Fourth member of the Leikoupo Formation
PZG	Pengzhou gas field
Leikoupo-4 <sup>3</sup>	Third submember of Leikoupo-4

## References

- Aftab, S., Moghadam, R.H., Leisi, A., 2023. New interpretation approach of well logging data for evaluation of Kern aquifer in South California. *J. Appl. Geophys.* 215, 105138. [https://doi.org/10.1016/j.jappgeo.2023](https://doi.org/10.1016/j.jappgeo.2023.105138).
- Algeo, T.J., 1993. Quantifying stratigraphic completeness: a probabilistic approach using paleomagnetic data. *J. Geol.* 101, 421–433. <https://doi.org/10.1002/2014JF003298>.
- Al-Siyabi, H.A., 2005. Exploration history of the Ara intrasalt carbonate stringers in the south Oman salt basin. *GeoArabia* (Manama) 10, 39–72. <https://doi.org/10.2113/geoarabia100439>.
- Bai, S., Kolter, J.Z., Koltun, V., 2018. An Empirical Evaluation of Generic Convolutional and Recurrent Networks for Sequence Modeling. *ArXiv*, abs/1803.01271.
- Barbosa, L.F.F.M., Nascimento, A., Mathias, M.H., et al., 2019. Machine learning methods applied to drilling rate of penetration prediction and optimization – a review. *J. Petrol. Sci. Eng.* 183, 106332. <https://doi.org/10.1016/j.petrol.2019.106332>.
- Bhatt, A., Helle, H.B., 2002. Determination of facies from well logs using modular neural networks. *Pet. Geosci.* 8 (3), 217–228. <https://doi.org/10.1144/petgeo.8.3.217>.
- Bhattacharya, S., Carr, T.R., Pal, M., 2016. Comparison of supervised and unsupervised approaches for mudstone lithofacies classification: case studies from the Bakken and Mahantango-Marcellus Shale, USA. *J. Nat. Gas Sci. Eng.* 33, 1119–1133. <https://doi.org/10.1016/j.jngse.2016.04.055>.
- Bressan, T.S., Kehl de Souza, M., Girelli, T.J., et al., 2020. Evaluation of machine learning methods for lithology classification using geophysical data. *Comput. Geosci.* 139, 104475. <https://doi.org/10.1016/j.cageo.2020.104475>.
- Busch, J.M., Fortney, W.G., Berry, L.N., 1987. Determination of lithology from well logs by statistical analysis. *SPE Form. Eval.* 2, 412–418. <https://doi.org/10.2118/14301-PA>.
- Cao, D., Wang, Y., Duan, J., Zhang, C., et al., 2020. Spectral temporal graph neural network for multivariate time-series forecasting. In: Proceedings of the 34th International Conference on Neural Information Processing Systems. Article 1491. <https://arxiv.org/abs/2103.07719>.
- Carrasquilla, A., 2023. Lithofacies prediction from conventional well logs using geological information, wavelet transform, and decision tree approach in a carbonate reservoir in southeastern Brazil. *J. S. Am. Earth Sci.* 128, 104431. <https://doi.org/10.1016/j.jsames.2023.104431>.
- Chawla, N.V., Bowyer, K.W., Hall, L.O., et al., 2002. SMOTE: synthetic minority oversampling technique. *J. Artif. Intell. Res.* 16, 321–357. <https://arxiv.org/abs/1106.1813>.
- Chen, T., Gao, G., Liu, H., et al., 2023. Rock brittleness index inversion method with constraints of seismic and well logs via a CNN-GRU fusion network based on the spatiotemporal attention mechanism. *Geoenergy Sci. Eng.* 225, 211646. <https://doi.org/10.1016/j.geoen.2023.211646>.
- Chen, W., Yang, L., Zha, B., et al., 2020. Deep learning reservoir porosity prediction using a multilayer long short-term memory network. *Geophysics* 85 (WA213-WA225). <https://doi.org/10.1190/geo2019-0261.1>.
- Cho, K., van Merriënboer, B., Gulcehre, C., et al., 2014. Learning phrase representations using RNN encoder-decoder for statistical machine translation. *Empirical Methods in Natural Language Processing*. <https://arxiv.org/abs/1406.1078>.
- Collins, J., Narr, W., Harris, P.M., et al., 2014. Lithofacies, depositional environments, burial diagenesis, and dynamic field behavior in a Carboniferous slope reservoir, Tengiz Field (Republic of Kazakhstan), and comparison with outcrop analogs. In: Verwer, K., Playton, T.E., Harris, P.M., Mitch (Eds.), *Deposits, Architecture, and Controls of Carbonate Margin, Slope and Basinal Settings*. SEPM Society for Sedimentary Geology. <https://doi.org/10.2110/sepmsp.105.11>.
- Dong, S., Wang, L., Zeng, L., et al., 2023a. Fracture identification in reservoirs using well log data by window sliding recurrent neural network. *Geoenergy Sci. Eng.* 230, 212165. <https://doi.org/10.1016/j.geoen.2023.212165>.
- Dong, S., Zhong, Z., Cui, X., 2023b. A deep kernel method for lithofacies identification using conventional well logs. *Pet. Sci.* 20 (4), 1411–1428. <https://doi.org/10.1016/j.petsci.2022.11.027>.
- Dubois, M.K., Bohling, G.C., Chakrabarti, S., 2007. Comparison of four approaches to a rock facies classification problem. *Comput. Geosci.* 33, 599–617. <https://doi.org/10.1016/j.cageo.2006.08.011>.
- Feng, Q.F., Xiao, Y.X., Hou, X.L., et al., 2021. A logging identification method for depositional facies in the Sinian Dengying Formation of the Sichuan Basin. *Pet. Sci.* 18, 1086–1096. <https://doi.org/10.1016/j.petsci.2020.10.002>.
- Feng, R., 2021. Uncertainty analysis in well log classification using Bayesian long short-term memory networks. *J. Petrol. Sci. Eng.* 205, 108816. <https://doi.org/10.1016/j.petrol.2021.108816>.
- Ghosh, S., Chatterjee, R., Shanker, P., 2016. Estimation of ash, moisture content, and detection of coal lithofacies from well logs using regression and artificial neural network modeling. *Fuel* 177, 279–287. <https://doi.org/10.1016/j.fuel.2016.03.001>.
- Graves, A., 2012. Long short-term memory. In: Graves, A. (Ed.), *Supervised Sequence Labelling with Recurrent Neural Networks*. Springer Berlin Heidelberg, pp. 37–45. [https://doi.org/10.1007/978-3-642-24797-2\\_4](https://doi.org/10.1007/978-3-642-24797-2_4).
- Grotzinger, J., Al-Rawahi, Z., 2014. Depositional facies and platform architecture of microbialite-dominated carbonate reservoirs, Ediacaran–Cambrian Ara Group, Sultanate of Oman. *AAPG (Am. Assoc. Pet. Geol.) Bull.* 98, 1453–1494. <https://doi.org/10.1306/02271412063>.
- Hall, B., 2016. Facies classification using machine learning. *Lead. Edge* 35, 906–909. <https://doi.org/10.1190/tle35100906.1>.
- Hilborn, R.C., 2000. Chaos and nonlinear dynamics: an introduction for scientists and engineers. [https://doi.org/10.1007/978-0-387-21562-4\\_14](https://doi.org/10.1007/978-0-387-21562-4_14).
- Hochreiter, S., Schmidhuber, J., 1997. Long short-term memory. *Neural Comput.* 9, 1735–1780. <https://doi.org/10.1162/neco.1997.9.8.1735>.
- Jiang, L., Hu, S., Zhao, W., et al., 2018a. Diagenesis and its impact on a microbially derived carbonate reservoir from the middle triassic Leikoupo Formation, Sichuan Basin, China. *AAPG (Am. Assoc. Pet. Geol.) Bull.* 102, 2599–2628. <https://doi.org/10.1306/05111817021>.
- Jiang, L., Worden, R.H., Cai, C.F., et al., 2018b. Diagenesis of an evaporite-related carbonate reservoir in deeply buried Cambrian strata, Tarim Basin, northwest China. *AAPG (Am. Assoc. Pet. Geol.) Bull.* 102, 77–102. <https://doi.org/10.1306/0328171608517048>.
- Jiang, L., Xu, Z., Shi, S., et al., 2019. Multiphase dolomitization of a microbialite-dominated gas reservoir, the middle triassic Leikoupo Formation, Sichuan Basin, China. *J. Petrol. Sci. Eng.* 180, 820–834. <https://doi.org/10.1016/j.petrol.2019.05.014>.
- Kannaiah, P.V.D., Maurya, N.K., 2023. Machine learning approaches for formation matrix volume prediction from well logs: insights and lessons learned. *Geoenergy Sci. Eng.* 229, 212086. <https://doi.org/10.1016/j.geoen.2023.212086>.
- Lan, C., Xu, Z., Yang, D., et al., 2022. Stratigraphy and depositional evolution of the terminal Ediacaran platform in the central to northern Sichuan Basin, Southwest China. *Palaeogeogr. Palaeoclimatol. Palaeoecol.* 601, 111142. <https://doi.org/10.1016/j.palaeo.2022.111142>.
- Lipton, Z.C., 2015. A critical review of recurrent neural networks for sequence learning. <https://arxiv.org/abs/1506.00019>.
- Liu, S., Deng, B., Jansa, L., et al., 2017. The early cambrian mianyang-changning intracratonic sag and its control on petroleum accumulation in the Sichuan Basin, China. *Geofluids* 2017, 6740892. <https://doi.org/10.1155/2017/6740892>.
- Liu, S., Yang, Y., Deng, B., et al., 2021. Tectonic evolution of the Sichuan Basin, southwest China. *Earth Sci. Rev.* 213, 103470. <https://doi.org/10.1016/j.earscirev.2020.103470>.
- Mancini, E.A., Llinás, J.C., Parcell, W.C., et al., 2004. Upper Jurassic thrombolite reservoir play in the northeastern Gulf of Mexico. *AAPG (Am. Assoc. Pet. Geol.) Bull.* 88, 1573–1602. <https://doi.org/10.1306/06210404017>.
- Mancini, E.A., Parcell, W.C., Ahr, W.M., et al., 2008. Upper Jurassic up-dip stratigraphic trap and associated Smackover microbial and nearshore carbonate facies in the eastern Gulf coastal plain. *AAPG (Am. Assoc. Pet. Geol.) Bull.* 92 (4), 417–442. <https://doi.org/10.1306/11140707076>.
- Passy, Q.R., Creaney, S., Kulla, J.B., Moretti, F.J., Stroud, J.D., 1990. A practical model for organic richness from porosity and resistivity logs. *AAPG Bulletin* 74 (12), 1777–1794. <https://doi.org/10.1306/0C9B25C9-1710-11D7-8645000102C1865D>.
- Pham, V., Bluche, T., Kermorvant, C., Louradour, J., 2014. Dropout improves recurrent neural networks for handwriting recognition. In: 2014 14th International Conference on Frontiers in Handwriting Recognition, pp. 285–290. <https://doi.org/10.1109/ICFHR.2014.55>.
- Prokoph, A., 1999. Fractal, multifractal, and sliding window correlation dimension analysis of sedimentary time series. *Comput. Geosci.* 25, 1009–1021. [https://doi.org/10.1016/S0098-3004\(99\)00063-1](https://doi.org/10.1016/S0098-3004(99)00063-1).
- Prokoph, A., Barthelmes, F., 1996. Detection of nonstationarities in geological time series: wavelet transform of chaotic and cyclic sequences. *Comput. Geosci.* 22, 1097–1108. [https://doi.org/10.1016/S0098-3004\(96\)00054-4](https://doi.org/10.1016/S0098-3004(96)00054-4).
- Rogers, S.J., Fang, J.H., Karr, C.L., et al., 1992. Determination of lithology from well logs using a neural network. *AAPG (Am. Assoc. Pet. Geol.) Bull.* 76 (5), 731–739. <https://doi.org/10.1306/BDF88BC-1718-11D7-8645000102C1865D>.
- Romanenkova, E., Rogulina, A., Shakirov, A., et al., 2022. Similarity learning for wells based on logging data. *J. Petrol. Sci. Eng.* 215, 110690. <https://doi.org/10.1016/j.petrol.2022.110690>.
- Shan, L., Liu, Y., Tang, M., Yang, M., Bai, X., 2021. CNN-BiLSTM hybrid neural

- networks with attention mechanism for well log prediction. *J. Petrol. Sci. Eng.* 205, 108838. <https://doi.org/10.1016/j.petrol.2021.108838>.
- Smodej, J., Reuning, L., Becker, S., et al., 2019. Micro- and nano-pores in intrasalt, microbialite-dominated carbonate reservoirs, Ara Group, South-Oman salt basin. *Mar. Petrol. Geol.* 104, 389–403. <https://doi.org/10.1016/j.marpetgeo.2019.03.036>.
- Song, T., Zhu, W., Chen, Z., et al., 2023. A novel well-loggin data generation model integrated with random forests and adaptive domain clustering algorithms. *Geoenergy Sci Eng.* 231, 212381. <https://doi.org/10.1016/j.geoen.2023.212381>.
- Souza, W.E., Cerqueira, A.G., Porsani, M.J., 2022. Seismic velocity field estimation using sonic well logs decomposed by Singular Spectrum Analysis (SSA) and Exponentially Weighted Moving Average (EWMA) - a case of study in Recôncavo Basin, Brazil. *J. Appl. Geophys.* 206, 104821. <https://doi.org/10.1016/j.jappgeo.2022.104821>.
- Srivastava, N., Hinton, G., Krizhevsky, A., et al., 2014. Dropout: a simple way to prevent neural networks from overfitting. *J. Mach. Learn. Res.* 15, 1929–1958. <https://dl.acm.org/doi/abs/10.5555/2627435.2670313>.
- Srivastava, N., Mansimov, E., Salakhutdinov, R., 2015. Unsupervised learning of video representations using LSTMs. *Proceedings 32nd Int Conf Machine Learn.* 37, 843–852. JMLR.org, Lille, France. <https://arxiv.org/abs/1502.04681>.
- Tang, H., Tan, X., Liu, H., et al., 2014. Genesis and dolomitization of "khai" powder crystal dolomite in triassic jialingjiang formation, Moxi gas field, central Sichuan Basin, SW China. *Petrol. Explor. Dev.* 41, 553–562. [https://doi.org/10.1016/S1876-3804\(14\)60066-5](https://doi.org/10.1016/S1876-3804(14)60066-5).
- Tang, P., Chen, D., Wang, Y., et al., 2022. Diagenesis of microbialite-dominated carbonates in the upper ediacaran qigebak formation, NW tarim basin, China: implications for reservoir development. *Mar. Petrol. Geol.* 136, 105476. <https://doi.org/10.1016/j.marpetgeo.2021.105476>.
- Verma, A.K., Routray, A., Mohanty, W.K., 2014. Assessing similarity between well logs using synchronization measures. *Geosci. Rem. Sens. Lett. IEEE* 11, 2032–2036. <https://doi.org/10.1109/LGRS.2014.2317498>.
- Wager, S., Wang, S., Liang, P.S., 2013. Dropout training as adaptive regularization. In: Burges, C.J., Bottou, L., Welling, M., Ghahramani, Z., Weinberger, K.Q. (Eds.), *Advances in Neural Information Processing Systems*. Curran Associates, Inc. <https://ieeexplore.ieee.org/book/6267330>.
- Wan, Z., Wei, F., Peng, J., et al., 2023. Application of physical model-based machine learning to the temperature prediction of electronic device in oil-gas exploration logging. *Energy* 282, 128973. <https://doi.org/10.1016/j.energy.2023.128973>.
- Wang, G., Carr, T.R., 2012. Methodology of organic-rich shale lithofacies identification and prediction: a case study from Marcellus Shale in the Appalachian Basin. *Comput. Geosci.* 49, 151–163. <https://doi.org/10.1016/j.cageo.2012.07.011>.
- Wang, J., Cao, J., Fu, J., et al., 2022. Missing well logs prediction using deep learning integrated neural network with the self-attention mechanism. *Energy* 261, 125270. <https://doi.org/10.1016/j.energy.2022.125270>.
- Wang, L., He, Y., Peng, X., et al., 2020. Pore structure characteristics of an ultradep carbonate gas reservoir and their effects on gas storage and percolation capacities in the Deng IV member, Gaoshiti-Moxi Area, Sichuan Basin, SW China. *Mar. Petrol. Geol.* 111, 44–65. <https://doi.org/10.1016/j.marpetgeo.2019.08.012>.
- Wei, G., Wang, D., Wang, X., et al., 2014. Characteristics of noble gases in the large Gaoshiti-Moxi gas field in Sichuan Basin, SW China. *Petrol. Explor. Dev.* 41, 585–590. [https://doi.org/10.1016/S1876-3804\(14\)60069-0](https://doi.org/10.1016/S1876-3804(14)60069-0).
- Worthington, P.F., 1990. Sediment Cyclicity Observed in Well Logs, vol. 48. Geological Society, London, Special Publications, pp. 123–132. <https://doi.org/10.1144/GSL.SP.1990.048.01.11>.
- Xiao, T., Li, H., Ouyang, W., et al., 2016. Learning deep feature representations with domain guided dropout for person Re-identification. In: 2016 IEEE Conference on Computer Vision and Pattern Recognition (CVPR), pp. 1249–1258. <https://doi.org/10.1109/CVPR.2016.140>.
- Xie, Y., Zhu, C., Zhou, W., et al., 2018. Evaluation of machine learning methods for identifying formation lithology: a comparison of tuning processes and model performance. *J. Petrol. Sci. Eng.* 160, 182–193. <https://doi.org/10.1016/j.petrol.2017.10.028>.
- Xu, Z., Shi, H., Lin, P., et al., 2021. Integrated lithology identification based on rock images and elemental data. *J. Petrol. Sci. Eng.* 205, 108853. <https://doi.org/10.1016/j.petrol.2021.108853>.
- Yan, R., Xu, G., Xu, F., et al., 2022. Multistage dissolution characteristics and their influence on mound-shoal complex reservoirs from the Sinian Dengying Formation in the southeastern Sichuan Basin, China. *Mar. Petrol. Geol.* 139, 105596. <https://doi.org/10.1016/j.marpetgeo.2022.105596>.
- Yang, W., Xia, K., Fan, S., 2023. Oil logging reservoir recognition based on TCN and SA-BiLSTM deep learning method. *Eng. Appl. Artif. Intell.* 121, 105950. <https://doi.org/10.1016/j.engappai.2023.105950>.
- Yarali, O., Kahraman, S., 2011. Drillability assessment of rocks using different brittleness values. *Tunn. Undergr. Space Technol.* 26, 406–414. <https://doi.org/10.1016/j.tust.2010.11.013>.
- Zaremba, W., Sutskever, I., Vinyals, O., 2014. Recurrent neural network regularization. arXiv: Neural and Evolutionary Computing. <https://arxiv.org/abs/1409.2329>.
- Zeeden, C., Ulfers, A., Pierdominici, S., et al., 2023. Downhole logging data for time series analysis and cyclostratigraphy. *Earth Sci. Rev.* 241, 104436. <https://doi.org/10.1016/j.earscirev.2023.104436>.
- Zhang, R., Zhang, C., Song, X., et al., 2023. Real-time prediction of logging parameters during the drilling process using an attention-based Seq2Seq model. *Geoenergy Sci Eng.*, 212279 <https://doi.org/10.1016/j.geoen.2023.212279>.
- Zhang, W., Shan, X., Fu, B., et al., 2022. A deep encoder-decoder neural network model for total organic carbon content prediction from well logs. *J. Asian Earth Sci.* 240, 105437. <https://doi.org/10.1016/j.jseaes.2022.105437>.
- Zheng, D., Hou, M., Chen, A., et al., 2022. Application of machine learning in the identification of fluvial-lacustrine lithofacies from well logs: a case study from the Sichuan Basin, China. *J. Petrol. Sci. Eng.* 215, 110610. <https://doi.org/10.1016/j.petrol.2022.110610>.
- Zhu, D., Liu, Q., He, Z., et al., 2020. Early development and late preservation of porosity linked to the presence of hydrocarbons in Precambrian microbialite gas reservoirs within the Sichuan Basin, southern China. *Precambr. Res.* 342, 105694. <https://doi.org/10.1016/j.precamres.2020.105694>.
- Zhu, D., Liu, Q., Wang, J., et al., 2022. Transition of seawater conditions favorable for the development of microbial hydrocarbon source-reservoir assemblage system in the Precambrian. *Precambr. Res.* 374, 106649. <https://doi.org/10.1016/j.precamres.2022.106649>.
- Zou, C., Du, J., Xu, C., et al., 2014. Formation, distribution, resource potential, and discovery of the Sinian-Cambrian giant gas field in the Sichuan Basin, southwest China. *Petrol. Explor. Dev.* 41, 306–325. [https://doi.org/10.1016/S1876-3804\(14\)60036-7](https://doi.org/10.1016/S1876-3804(14)60036-7).